SEISMIC SIGNATURES OF PORE CONNECTIVITY

A Dissertation

Presented to

the Faculty of the Department of Earth and Atmospheric Sciences

University of Houston

In Partial Fulfillment

of the Requirements for the Degree

Doctor of Philosophy

By

Rui Zhou

August 2014

SEISMIC SIGNATURES OF PORE CONNECTIVITY

Rui Zhou

APPROVED:

Dr. Evgeny Chesnokov, Chairman
Department of Earth and Atmospheric Sciences

Dr. Gennady Goloshubin
Department of Earth and Atmospheric Sciences

Dr. Arthur Weglein
Department of Earth and Atmospheric Sciences

Dr. Dileep Tiwary
Chevron

Dean, College of Natural Sciences and Mathematics

Acknowledgements

This dissertation would not have been possible without the help of the people at our department.

My advisor, Dr. Evgeny Chesnokov, allows me to work on this interesting topic and give me many stimulating theoretical discussions with regard to general singular approximation (GSA), anisotropy, and porous medium. I would never be able to finish without his help, encouragement, guidance, and tolerance.

I appreciate Dr. Gennady Goloshubin, Dr. Arthur Weglein, and Dr. Dileep Tiwary for taking time to serve as my committee members and raising very interesting questions.

Special thanks to Dr. Irina Bayuk, Dr. Tao Jiang, and Dr. Luanxiao Zhao for discussions with GSA. Dr. Irina Bayuk gave several E-mail replies to my inquiry of the concept of friability and Dr. Tao Jiang taught me some steps in deriving GSA. Mr. Kefei Lu and Dr. Yasser Metwally's discussions of their experimental data are appreciated. I thank Dr. Gennady Goloshubin for discussions of poroelasticity and viscoelasticity and Dr. Leon Thomsen for discussions of anisotropy. I appreciate Dr. Luanxiao Zhao and Dr. Malleswar Yenugu for proof reading my proposal. I appreciate Dr. Patrick Rasolofosaon for sending his doctoral dissertation to me and Dr. Haitao Ren for answering my several E-mail questions to his paper.

Finally, I thank Dr. Xiangwei Yu, Dr. Yuanze Zhou, and Dr. Nicolas Coltice for writing recommendation letters for my admission to University of Houston .

SEISMIC SIGNATURES OF PORE CONNECTIVITY

An Abstract of a Dissertation

Presented to

the Faculty of the Department of Earth and Atmospheric Sciences

University of Houston

In Partial Fulfillment

of the Requirements for the Degree

Doctor of Philosophy

By

Rui Zhou

August 2014

Abstract

The goal of this dissertation is analyzing medium parameters influence on seismic signatures, especially pore connectivity. Firstly, I use the Zoeppritz equation to analyze reflection coefficient's sensitivity to eight medium parameters; results show they all have significantly different sensitivity.

Friability is an empirical parameter introduced in General Singular Approximation (GSA) to measure the extent of pore connectivity that has the numerical range from 0 to 1. In the second part, with other assumed medium parameters, calculation results show friability has observable seismic signatures. Most of them have very large, non-monotonic, and nonlinear variations to friability. Specifically, I observe: 1, as friability increases, most stiffness-tensor components decrease; 2, most extended Thomsen's parameters decrease as friability increases. ϵ^2, γ^2, δ^2, and δ^3 in gas-saturated medium and ϵ^1, δ^2, and δ^3 in water-saturated medium are very sensitive to friability, while others are not; 3, there are sophisticated relationships between phase velocities and friability out of the symmetry plane, especially for S_2 wave; 4, friability equals zero corresponds to the largest critical angle, while friability equals 1 corresponds to the smallest. Critical angle mostly increases as azimuth angle increases; 5, normal incident PP reflection coefficient is enough to detect the friability variation in gas-saturated medium. On the other hand, azimuthal variation of PP reflection coefficient also depends strongly on friability in both media.

Lastly, as a comparison to GSA, poroviscoelasticity is introduced by synthesizing Biot theory and viscoelasticity because Biot theory assumes completely-connected pore space. The influence of frame inelasticity on poroviscoelastic wave dispersions, attenuations, and reflection and transmission coefficients are computed and analyzed in detail. Results show frame inelasticity has considerable influence on reflection and transmission coefficients in certain frequencies and incidence angles.

Contents

List of Figures

List of Tables

Chapter 1

Introduction to the Dissertation

In recent years, the influence of pore connectivity (Agersborg et al., 2008), pore structure (Sun, 2004), and permeability (Rubino et al., 2012; Pride et al., 2003) on seismic signatures received much attention. Pore structure is a transport property that is important in shale-gas exploration because it is directly related to permeability, one of the key factors for oil production. Hydraulic fracturing is also related to the subsurface pore structure, especially pore connectivity. After hydraulic fracturing, the pore connectivity increases, which is reflected in surface or downhole seismic and logging data. These data, especially seismic reflection amplitude, are useful for inverting the pore structure.

Thus, the problem lies in choosing a specific method to invert the pore structure. Although the final determination of which reflection-amplitude-computation scheme is best should be based on experimental results, numerical comparisons of various methods are still helpful for understanding the different schemes, especially when the different schemes are applied to study the same rock. Among the different schemes, anisotropy and Biot theory are two very popular ones. Consequently, this work studies the influence of pore connectivity on seismic signatures in the frame of anisotropy and Biot theory. In the anisotropy framework, the incorporation of pore connectivity is through the empirical parameter friability (Bayuk and Chesnokov, 1998; Bayuk and Rodkin, 1999; Tiwary, 2007; Jiang, 2013) in General Singular Approximation (GSA) that has the numerical range from 0 to 1. Furthermore, Biot (1956a,b) theory characterizes connected pore space, it assumes fluid flow in a connected tube and includes Darcy's law in the theory.

The comparison between isotropic elasticity and Biot theory from the perspective of reflection and transmission (hereafter shorten as R/T) coefficients has been shown in Bouzidi and Schmitt (2012). They also did an experiment which shows the Biot reflection modeling is more accurate than elastic R/T modeling. In their work, the upper layer is water. However, in geophysical exploration, the different layers mostly consist of solid rocks with various kinds of pore and fracture. Consequently, different methods are needed for computing R/T coefficients in realistic earth models.

1.1 Introduction to the chapters

In Chapter 2 of the dissertation, I study the reflection coefficient variation with ρ, V_P, V_S, μ, λ, K, ν, and E with Zoeppritz equations. My results show different parameterization leads to significantly different medium parameter's sensitivity to reflection coefficient. This simple work is necessary for understanding reflection coefficient before sophisticated modeling.

In Chapter 3, General Singular Approximation is used to model friability's influence on stiffness-tensors, extended Thomsen's parameters, phase velocities, critical angles, and PP reflection coefficients. I find most of these signatures have very large, non-monotonic, and nonlinear variations to friability variations.

In Chapter 4, by introducing frame inelasticity into Biot theory that generates the poroviscoelastic model, I study frame inelasticity's influence on poroviscoelastic dispersions, attenuations, and reflections. The computation are based on Gulf of Mexico sand. In some frequency and incidence angle, graphically illustrated results show frame inelasticity has considerable influence on reflection and transmission coefficients.

Chapter 2

Zoeppritz Reflectivity Variations with Eight Medium Parameters

2.1 Introduction

The main content of my dissertation involves anisotropic and poroviscoelastic characterizations of rocks. Before these comprehensive studies, a study of the simpler situation gives us a simpler understanding of reflectivity, which is also easier to implement. The second chapter focus on forward modeling of SH, PP, and PSV reflection coefficient magnitudes (hereafter refer as RCM) variation to medium parameters ρ, V_P, V_S, μ, λ, K, ν, and E in isotropic, homogeneous, and lossless medium. Although these parameters are probably not very directly related to the existence of oil or gas or the generation of earthquakes, I choose them because they are the most fundamental parameters for characterizing a medium and they also have very clear physical meanings.

The development of the theoretical part of this chapter has a long history. Green (1848) revised the molecular formulation of elasticity and introduce the concept of strain energy that allows him to study the reflection and transmission (hereafter refer as R/T) of light. Knott (1888) is the first to explicitly account for the partition of wave energy along plane boundary. Zoeppritz (1919) derived the modern form of plane wave R/T coefficients which make the method named after him as "Zoeppritz equations", which is the main topic of this chapter. After Zoeppritz, there were many studies of his equations in different forms or simplifications (Jakosky, 1950; Shuey, 1985; Hilterman, 2001; Aki and Richards, 2009). For a comprehensive list of papers with different forms, see Table 1 of Young and Braile (1976). Aki and Richards (2009) gave a concise and exact formulation. In this chapter, I follow their approach. Except for a different sign of SV wave potential definition, their formulas are equal to Jakosky (1950).

Koefoed (1955) noticed the direct influence of Poisson's ratio on reflection coefficient, which is one of the reasons that motivated Shuey (1985) to test the PP wave reflection coefficient to Poisson's ratio with a whole range of incidence angle (offset) of gas sands with exact Zoeppritz equations and his approximate formulas. Koefoed (1962) solved the Zoeppritz equations with different contrasts of velocity, density, and Poisson's ratio up to 90° of incidence angle and give many tables. Probably due to the computational power at that time, their sampling rate of media parameters and incidence angle were very large. Here, I have reduced the sampling rate of medium parameters and incidence angle greatly. Domenico (1974) tested the sensitivity of water saturation on reflection coefficient based on Zoeppritz equations. Ostrander (1984) also tested the sensitivity of normal incident PP wave reflection coefficients to Poisson's ratio of gas sands.

Although medium parameters' influence on AVO can be converted into the previously mentioned eight parameters, I study them directly and simultaneously, and analyze the variation of RCMs to the eight parameters of a specific rock. On the other hand, although there are many simplifications or approximations, exact Zoeppritz equation are still widely used in modeling and inversion, especially with today's computing power. Furthermore, recent advancements in seismic exploration has made large-offset AVO or amplitude variation with phase modeling or inversion possible (Downton and Ursenbach, 2006; Skopintseva et al., 2011; Zhu and McMechan, 2012). On that account, I include over-critical-angle incidence here. I use the Barnett shale because gas shale is currently a hot seismic exploration object.

Here, I first give a brief description of the method for calculating SH, PP, and PSV reflection coefficients including boundary conditions, then I give numerical results of the variation of SH, PP, and PSV RCMs to some or all of the previously mentioned eight parameters. Finally, I summarize the numerical results with tables and in conclusions.

2.2 SH wave incidence

I first show SH wave incidence between two isotropic, homogeneous, and lossless media, which is simpler than P wave incidence. For the SH wave, see Figure 2.1(a) for schematic illustration of plane incident, reflected, and refracted waves. Due to SH wave polarization, I have the continuity of displacement and stress boundary conditions:

$$u_y^I = u_y^{II}$$

$$\sigma_{yz}^I = \sigma_{yz}^{II}$$

Also due to its polarization, SH wave incidence only generates reflected and transmitted SH waves. From the assumption of periodic plane waves, using Helmholtz decomposition of displacements, and after manipulations of boundary conditions, I have the reflected and transmitted SH wave displacements calculation equation as:

$$\begin{pmatrix} 1 & -1 \\ \frac{\mu_1 \cos\alpha}{V_{S1}} & \frac{\mu_2 \cos\alpha'}{V_{S2}} \end{pmatrix} \begin{pmatrix} A_1 \\ A_2 \end{pmatrix} = \begin{pmatrix} -1 \\ \frac{\mu_1 \cos\alpha}{V_{S1}} \end{pmatrix} \tag{2.1}$$

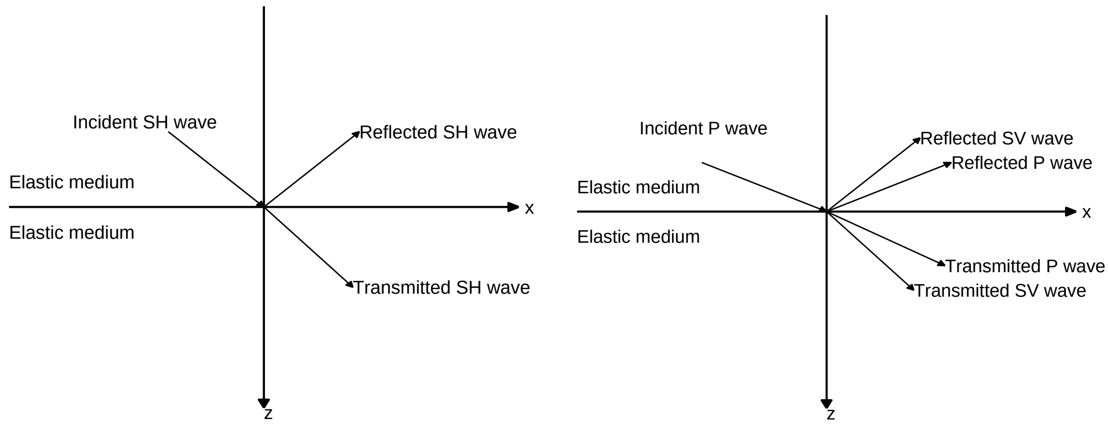

(a) (b)

Figure 2.1: Schematic diagrams of wave reflection and transmission between two homogeneous, isotropic, and lossless media for (a) SH wave with one reflected and one transmitted wave and (b) P wave with two reflected and two transmitted waves.

Algebraic manipulation of equation 2.1 yields the explicit form:

$$A_1 = \frac{V_{S2}\mu_1 \cos\alpha - V_{S1}\mu_2 \cos\alpha'}{V_{S2}\mu_1 \cos\alpha + V_{S1}\mu_2 \cos\alpha'}$$

$$A_2 = \frac{2V_{S2}\mu_1 \cos\alpha}{V_{S2}\mu_1 \cos\alpha + V_{S1}\mu_2 \cos\alpha'}$$

In these equations, A_1, A_2, α, $\alpha^{'}$, μ_1, μ_2, V_{S1}, and V_{S2} mean R/T coefficients, angle of incident and reflected waves, angle of transmitted wave, shear modulus of the upper layer, shear modulus of the lower layer, shear velocity of the upper layer, and shear velocity of the lower layer, respectively.

From the direct application of the equation of Snell's law, an incident wave may causes the sine of reflected or transmitted angles bigger than 1. In this situation, complex number must be introduced to the value of cosine of reflected or transmitted angle, and we have inhomogeneous reflected or transmitted waves. Taking the transmitted angle α' as an example (See Figure 2.1(a)), if the velocity of the incident medium is bigger than the transmitted medium, the transmitted wave is parallel to the interface at certain incidence angles, at which point the incident angle is called critical angle. When the incidence angle is bigger than critical angle, from

Table 2.1: Average medium parameter values from 13 measured Barnett shale samples. The unit of ρ is Kg/m^3 and the units of V_P and V_S are m/s.

ρ	V_P	V_S
2575	4334	2553

Table 2.2: Upper and lower layers parameters made from Table 2.2. ρ, V_P, and V_S are approximations to Table 2.2, the other parameters are calculated from ρ, V_P, and V_S. The analysis of RCMs are from the variation of the lower layers parameters. The unit of ρ is Kg/m^3, the units of V_P and V_S are m/s, ν is dimensionless, and the units of μ, λ, K, ν, and E are GPa.

	ρ	V_P	V_S	μ	λ	K	ν	E
Upper	2500	4300	2500	15.625	14.975	25.39	0.2447	38.90
Lower	2600	4400	2600	17.576	15.184	26.90	0.2317	43.30

Snell's law $\sin\alpha' > 1$, thus $\cos\alpha' = \sqrt{1 - \sin^2\alpha'}$ should be positive or negative pure imaginary number. Given the directions of wave propagation and coordinate system, because wave can't have infinite amplitude, I choose positive pure imaginary number.

Using the 13 measured Barnett shale samples (Lu, 2012), I calculate their average density and velocity and make Table 2.2. Upper and lower layers parameters in Table 2.2 approximate Table 2.2. Table 2.2 has a small jump between upper and bottom layers, which are common for realistic geological situations. From the above equations and Table 2.2, I calculate the variation of SH wave RCMs through changing the medium parameters. Figure 2.2 shows the calculation results of SH wave incidence.

Similarly to Koefoed (1955), I draw general comments and descriptions about the variation of SH wave RCMs to medium parameters in Table 2.3, which can be

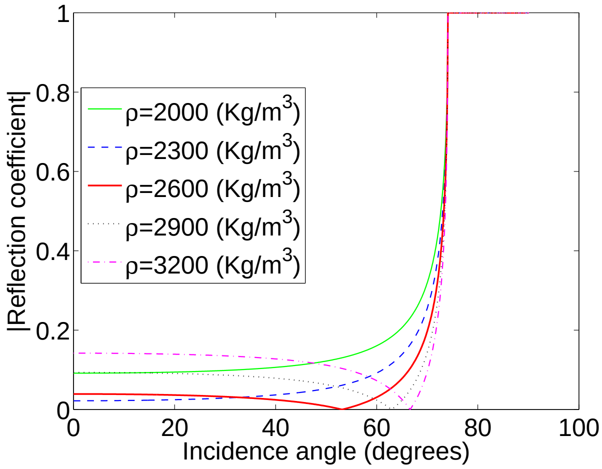

(a)

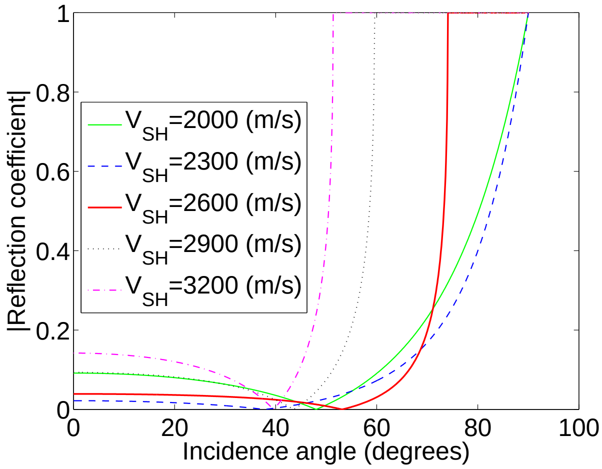

(b)

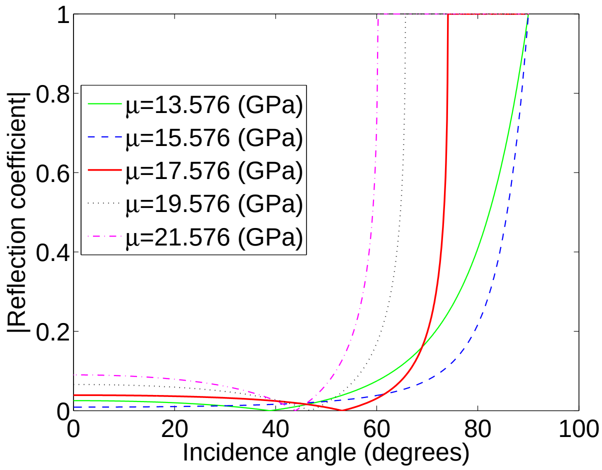

(c)

Figure 2.2: SH wave RCMs variation to bottom layer medium parameters with (a) ρ changes, μ changes by $\mu = \rho V_S^2$, and V_S is kept as constant, (b) V_S changes, μ changes by $\mu = \rho V_S^2$, and ρ is kept as constant, and (c) μ changes, V_S changes by $V_S = \sqrt{\frac{\mu}{\rho}}$, and ρ is kept as constant.

Table 2.3: SH wave RCMs variation to medium parameters. NI means normal incidence, $\uparrow$ means increase, $\downarrow$ means decrease, $\rightarrow$ means move to the right, $\leftarrow$ means move to the left, $\Rightarrow$ means change of variation direction, — means no variation, and $\bigcirc$ stands for inapplicable.

	NI	Over NI to zero RCM	Zero RCM	Over zero RCM	TIR starting point	Overall properties
$\rho\uparrow$		Very smooth at small offset compared with V_S and μ variation	$\rightarrow$	No crossover of RCMs	—	1, from NI to zero RCMs: RCMs are small and decrease smoothly into zero. 2, for over zero RCMs, RCMs increase rapidly from zero to one. 3, RCMs either increase monotonically to one or first decrease to zero then increase to one. 4, all RCMs are very similar except two cases of ρ decrease.
$V_S\uparrow$	$\downarrow\Rightarrow\uparrow$	Cross at relatively large offset compared with ρ and μ variation, more sensitive than μ variation	$\leftarrow\Rightarrow$ $\rightarrow\Rightarrow\leftarrow$	RCMs cross	$\leftarrow$	
$\mu\uparrow$		Relatively small RCMs compared with ρ and V_S variation	$\leftarrow\Rightarrow$ $\rightarrow\Rightarrow\leftarrow$	RCMs cross	$\leftarrow$	

used as a reference point for analyzing realistic data. In this test, it seems that ρ is the parameter that is most sensitive to SH wave RCM. We can see Figures 2.2(b) and 2.2(c) are very similar, which comes from the shear wave velocity-shear modulus relationship.

2.3 P wave incidence

For P wave incidence, similar to the SH wave reflection situation, the boundary conditions are:

$$u_x^I = u_x^{II} \text{ and } u_z^I = u_z^{II}$$

$$\sigma_{xz}^I = \sigma_{xz}^{II} \text{ and } \sigma_{zz}^I = \sigma_{zz}^{II}$$

See Figure 2.1(b) for schematic diagram for the R/T response of incident P wave. With similar process of solving the SH wave reflection problem, I can get the equations for calculating PP and PSV reflection coefficients as:

$$\begin{pmatrix} -\sin\alpha & -\cos\beta & \sin\alpha' & \cos\beta' \\ \cos\alpha & -\sin\beta & \cos\alpha' & -\sin\beta' \\ 2\rho_1 V_{S1}^2 p\cos\alpha & \rho_1 V_{S1}(1-2V_{S1}^2p^2) & 2\rho_2 V_{S2}^2 p\cos\alpha' & \rho_2 V_{S2}(1-2V_{S2}^2p^2) \\ -\rho_1\alpha_1(1-2V_{S1}^2p^2) & 2\rho_1 V_{S1}^2 p\cos\beta & \rho_2 V_{P2}(1-2V_{S2}^2p^2) & -2\rho_2 V_{S2}^2 p\cos\beta' \end{pmatrix} = M \quad (2.2)$$

$$M \times \begin{pmatrix} A_1 \\ A_2 \\ A_3 \\ A_4 \end{pmatrix} = \begin{pmatrix} \sin\alpha \\ \cos\alpha \\ 2\rho_1 V_{S1}^2 p\cos\alpha \\ \rho_1\alpha_1(1-2V_{S1}^2p^2) \end{pmatrix} \quad (2.3)$$

In these equations, A_1, A_2, α, $\alpha^{'}$, β, $\beta^{'}$, and p correspond to PP and PSV reflection coefficients, angle of reflected P wave, angle of reflected SV wave, angle of transmitted P wave, angle of transmitted SV wave, and ray parameter, respectively. Subscript 1 and 2 under ρ and V correspond to upper and lower layers, subscript P and S correspond to P and S waves. The meanings of other parameters are similar to equation 2.1. Notice the absolute values of the first column of the left side equals the absolute values of the right side: the first and fourth rows have opposite sign, and the second and third rows have the same sign.

We can see from equations 2.2 and 2.3 this medium is characterized by two independent parameters V_P and V_S plus density. Any other parameters are converted into the two independent parameters for input. See Figures 2.3, 2.4, 2.5, and 2.6 for calculation results.

The relationship between V_P, V_S, and ρ and other medium parameters are (Mavko et al., 2003):

$$K = \rho(V_P^2 - \frac{4}{3}V_S^2), \lambda = \rho(V_P^2 - 2V_S^2), E = \rho V_S^2 \frac{3V_P^2 - 4V_S^2}{V_P^2 - V_S^2}, \text{and } \nu = \frac{V_P^2 - 2V_S^2}{2(V_P^2 - V_S^2)} \tag{2.4}$$

So the process of varying medium parameters are:

1, for V_P, V_S, and ρ, vary them directly and put into equations 2.2 and 2.3.

2, for μ, vary μ and keep ρ as constant, then calculate V_S from μ and ρ to input into equations 2.2 and 2.3.

3, for K, λ, E, and ν, vary them and keep ρ as constant, then either calculate V_P and keep V_S as constant or calculate V_S and keep V_P as constant, then use V_P, V_S, and ρ as input to equations 2.2 and 2.3.

Step 2 is straightforward and step 3 is through converting equation 2.4: 1, for constant V_P, from equation 2.4, I have: $4\rho V_S^4 - (E + 3\rho V_P^2)V_S^2 + EV_P^2 = 0$, thus I have two corresponding shear velocities for some particular V_P and E:

$$V_S = \sqrt{\frac{E + 3\rho V_P^2 \pm \sqrt{(E + 3\rho V_P^2)^2 - 16\rho E V_P^2}}{8\rho}} \tag{2.5}$$

the negative sign is chosen due to the the proximity of calculated results to original E value. Figure 2.7 shows the variation of E with V_S when ρ and V_P are kept as constant, from which we can see E has a maximum value, thus only four instead of five variations of E are shown. Also:

$$V_S = \sqrt{\frac{3}{4}(V_P^2 - \frac{K}{\rho})} \tag{2.6a}$$

$$V_S = \sqrt{\frac{\rho V_P^2 - \lambda}{2\rho}} \tag{2.6b}$$

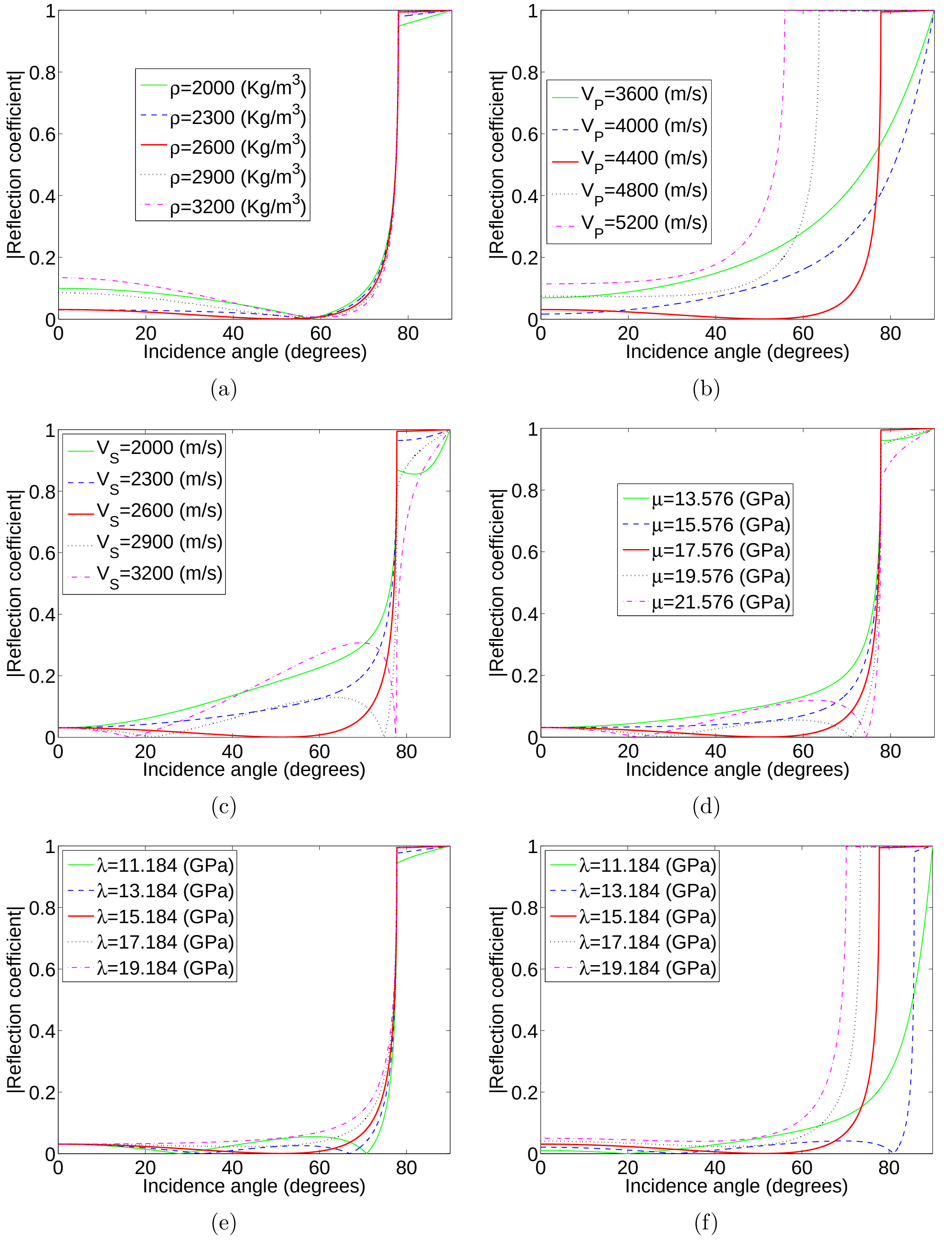

Figure 2.3: PP wave RCMs variation to bottom layer medium parameters with (a) ρ changes, (b) V_P changes, (c) V_S changes, (d) μ changes, V_S changes by $V_S = \sqrt{\frac{\mu}{\rho}}$, (e) λ changes, V_S changes by equation 2.6b, and (f) λ changes, V_P changes by equation 2.7c.

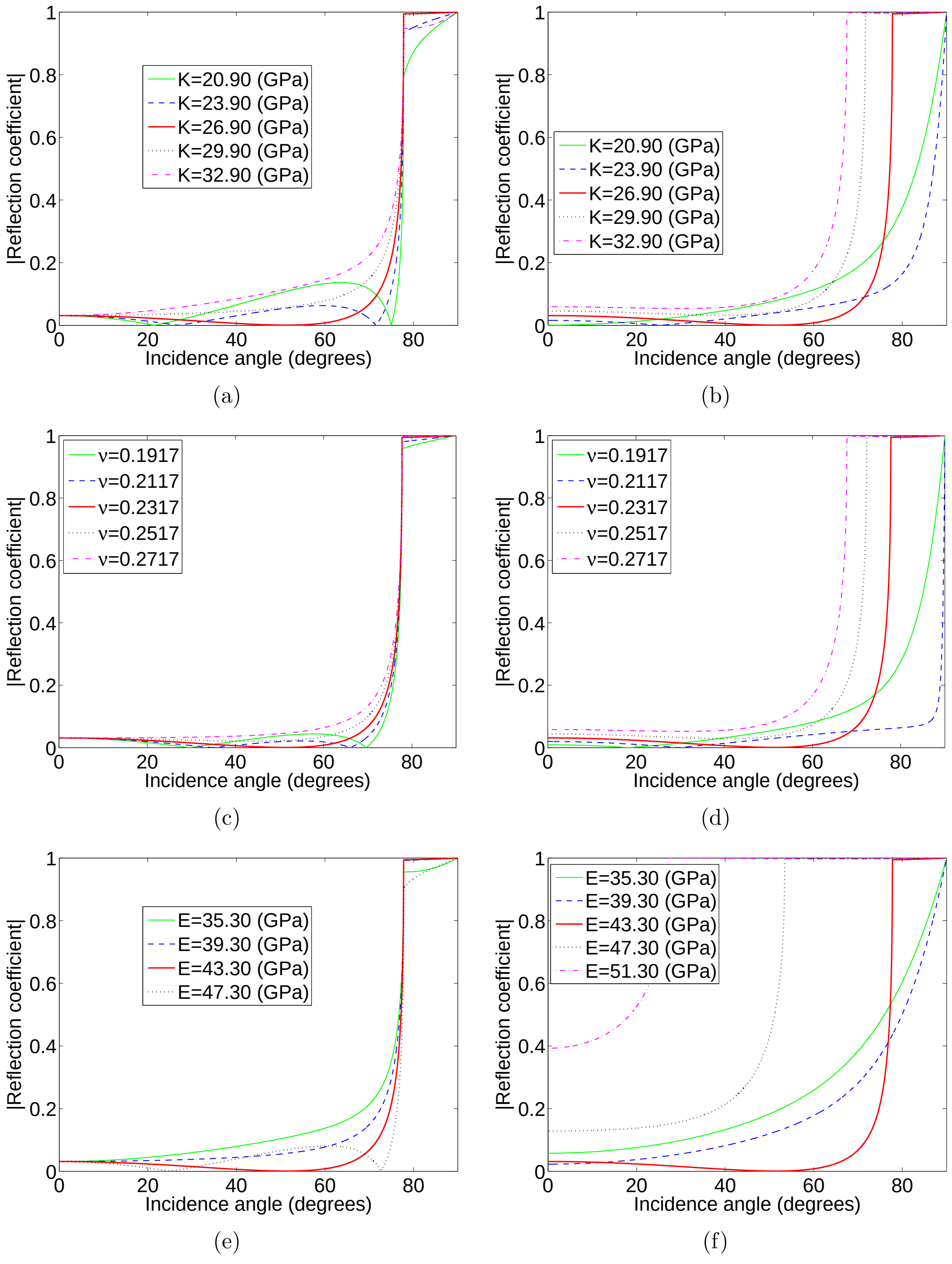

Figure 2.4: PP wave RCMs variation to bottom layer medium parameters with (a) K changes, V_S changes by equation 2.6a, (b) K changes, V_P changes by equation 2.7b, (c) ν changes, V_S changes by equation 2.6c, (d) ν changes, V_P changes by equation 2.7d, (e) E changes, V_S changes by equation 2.5, and (f) E changes, V_P changes by equation 2.7a.

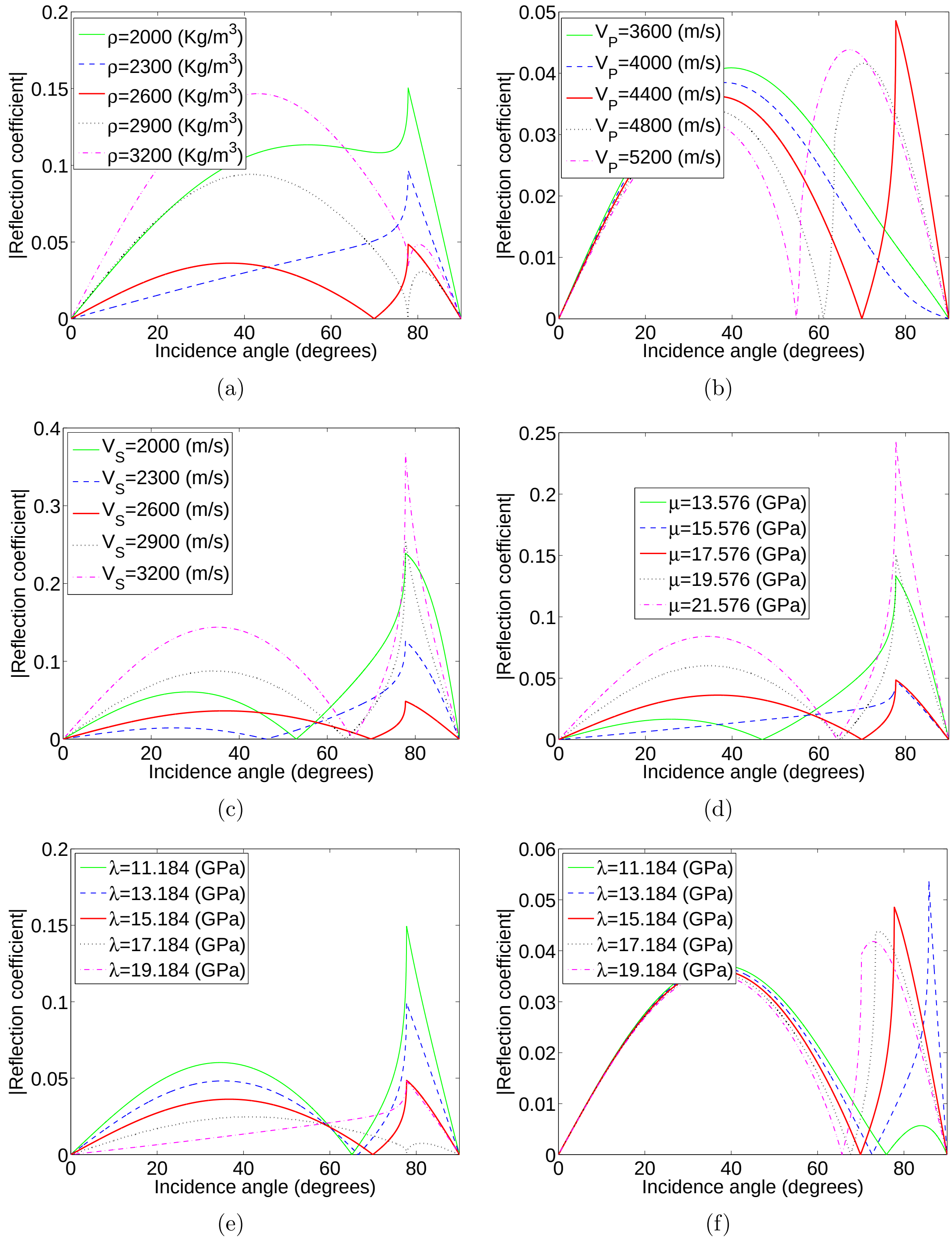

Figure 2.5: PSV wave RCMs variation to bottom layer medium parameters with (a) ρ changes, (b) V_P changes, (c) V_S changes, (d) μ changes, V_S changes by $V_S = \sqrt{\frac{\mu}{\rho}}$, (e) λ changes, V_S changes by equation 2.6b, and (f) λ changes, V_P changes by equation 2.7c.

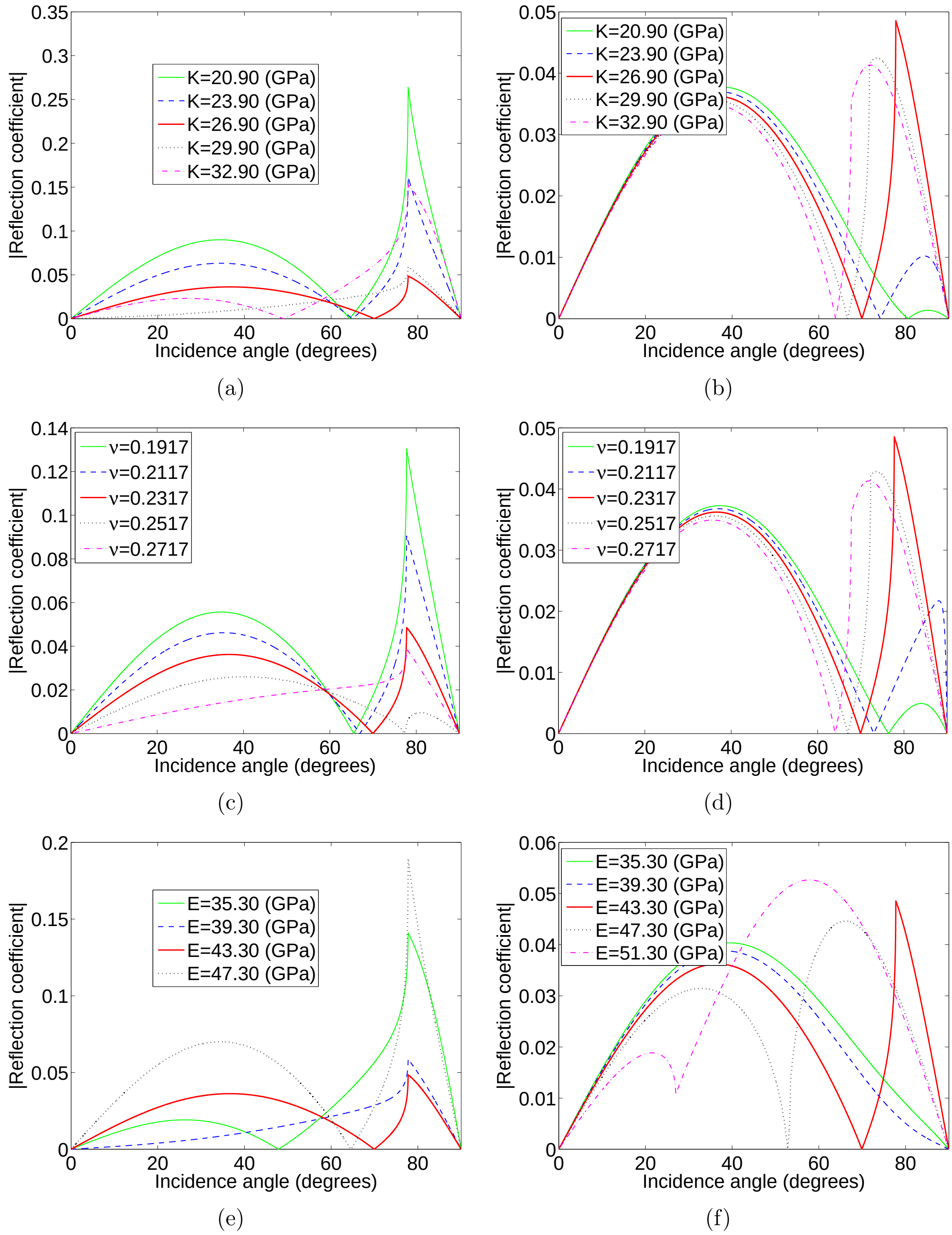

Figure 2.6: PSV wave RCMs variation to bottom layer medium parameters with (a) K changes, V_S changes by equation 2.6a, (b) K changes, V_P changes by equation 2.7b, (c) ν changes, V_S changes by equation 2.6c, (d) ν changes, V_P changes by equation 2.7d, (e) E changes, V_S changes by equation 2.5, and (f) E changes, V_P changes by equation 2.7a.

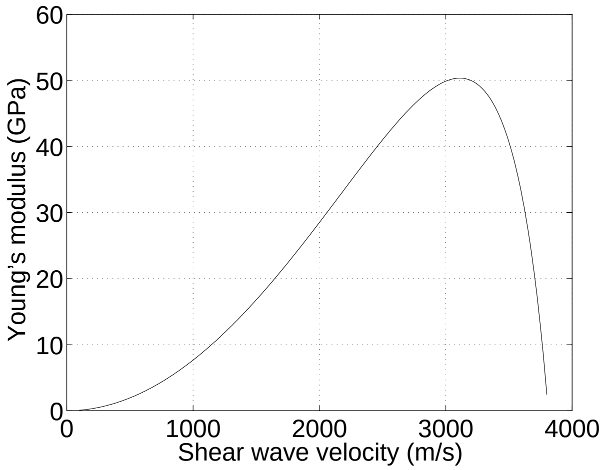

Figure 2.7: Variations of E with V_S when ρ and V_P are kept as constant.

$$V_S = V_P \sqrt{\frac{1-2\nu}{2(1+\nu)}} \tag{2.6c}$$

2, for constant V_S, I have:

$$V_P = \sqrt{\frac{(E-4\rho V_S^2)V_S^2}{E-3\rho V_S^2}} \tag{2.7a}$$

$$V_P = \sqrt{\frac{K}{\rho} + \frac{4}{3}V_S^2} \tag{2.7b}$$

$$V_P = \sqrt{\frac{\lambda + 2\rho V_S^2}{\rho}} \tag{2.7c}$$

$$V_P = V_S \sqrt{\frac{2(1+\nu)}{1-2\nu}} \tag{2.7d}$$

Here I show the characteristics of variation of PP wave RCM to medium parameters in Table 2.4 and PSV wave in Table 2.5. It is not easy to determine the zero of RCMs analytically (Levin, 1986), so here the determination of zero RCMs is through visual inspection of the numerical results.

It seems for PP RCMs, many occurrences of total internal reflection happens. However, this is an illusion. When I change the value of V_P of the underlying

Table 2.4: PP wave RCMs variation to medium parameters, see Table 2.3 caption for meanings of symbols. Descriptions of RCMs cross at small and large offset are relative in terms of the specified range.

Case	NI	Over NI to first zero RCM or 30° if no zero RCM	Zero RCM	Over first zero RCM or 30° if no zero RCM
1, $\rho\uparrow$	$\downarrow\Rightarrow\uparrow$	Can be relatively large at small offset, cross at small and large offset, and all decrease with increasing offset	$\leftarrow$	1, very irregular variation compared to near offset and highly frequently cross each other. 2, at large offset long range of PP RCMs are near one which means almost all the energy of incident waves are carried away by PP RCMs. 3, most cases have gradient discontinuities.
2, $V_P\uparrow$	$\downarrow\Rightarrow\uparrow$	Can be relatively large at small and large offset and cross at intermediate offset	$\bigcirc$	
3, $V_S\uparrow$	—	$\downarrow$ and small	$\leftarrow$	
4, $\mu\uparrow$	—	Similar to case 3	small offset: $\leftarrow$ large offset: $\rightarrow$	
5, $\lambda\uparrow, V_P$—	—	$\uparrow$ and small	small offset: $\rightarrow$ large offset: $\leftarrow$	
6, $\lambda\uparrow, V_S$—	$\uparrow$	$\uparrow$, small, and all decrease with increasing offset	$\rightarrow$	
7, $K\uparrow, V_P$—	—	Similar to case 5	Same as case 5	
8, $K\uparrow, V_S$—	$\uparrow$	Somewhat similar to case 6 except green solid line cross other lines at large offset	$\bigcirc$	
9, $\nu\uparrow, V_P$—	—	Similar to case 5	Same as case 5	
10, $\nu\uparrow, V_S$—	$\uparrow$	Similar to case 6	$\rightarrow$	
11, $E\uparrow, V_P$—	—	Somewhat similar to case 3 except black dotted line has zero RCM and magenta dash-dot line has no zero RCM and cross others at large offset	$\bigcirc$	
12, $E\uparrow, V_S$—	$\downarrow\Rightarrow\uparrow$	Somewhat similar to case 2 except black dotted line and blue dashed line don't cross	$\bigcirc$	

Table 2.5: PSV wave RCMs variation to medium parameters, see Table 2.3 caption for meanings of symbols.

Case	Over NI to first zero RCM	Zero RCM	Over zero RCM
1, $\rho \uparrow$	Can be relatively large and cross at intermediate offset	$\rightarrow$	1, Highly irregular variation compared to near offset and highly frequently cross each other; 2, The maximum RCM is almost the same as the corresponding maximum RCM at near offset for all cases; 3, All cases have gradient discontinuities.
2, $V_P \uparrow$	$\downarrow$, small, and no crossing	$\leftarrow$	
3, $V_S \uparrow$	Can be relatively large and cross at large offset	$\leftarrow\Rightarrow$ $\rightarrow\Rightarrow\leftarrow$	
4, $\mu \uparrow$	Similar to case 3	$\rightarrow\Rightarrow\leftarrow$	
5, $\lambda \uparrow, V_P$—	Small and cross at large offset	$\rightarrow$	
6, $\lambda \uparrow, V_S$—	Similar to case 2	$\leftarrow$	
7, $K \uparrow, V_P$—	Can be relatively large and cross at large offset	$\rightarrow\Rightarrow\leftarrow$	
8, $K \uparrow, V_S$—	Similar to case 2	$\leftarrow$	
9, $\nu \uparrow, V_P$—	Similar to case 5	$\rightarrow$	
10, $\nu \uparrow, V_S$—	Similar to case 2	$\leftarrow$	
11, $E \uparrow, V_P$—	Similar to case 7	$\rightarrow\Rightarrow\leftarrow$	
12, $E \uparrow, V_S$—	Somewhat similar to case 2 except magenta dash-dot line with discontinuous gradient cross other RCMs at large offset	$\leftarrow$	

medium, any of the V_S is smaller than the upper layer V_P, total internal reflection can't happen; when I change the value of V_S of the underlying medium, calculated results show none of the V_S is greater than the upper layer V_P, total internal reflection can't happen either. And it is obvious that total internal reflection can't happen for PSV RCMs. In consequence, total internal reflection can't happen for any of the RCMs.

2.4 Discussion

This chapter is not intended to be exhaustive. I only calculate and analyze PP and PSV RCMs for they are much more important than SVP and SVSV RCMs, and transmission coefficients are also ignored. Further, it is impossible to test all the possible combinations of medium parameters, I only give a brief extent of the possible combinations and limit the medium parameters variation to the bottom layer. Lastly, I only consider the magnitude for the sake of simplicity. Further work can test the variation in other domain such as τ-p.

2.5 Conclusions

I have calculated PP, PSV, and SH wave RCMs and listed their features in Tables 2.3, 2.4, and 2.5.

Additional properties of SH RCMs are:

1, total internal reflection always happen for over the critical angle incidence because inhomogeneous wave carries no energy;

2, for 90° incidence angles, RCMs equal one, which corresponds to total internal reflection.

Additional properties of PP RCMs are:

1, all maximum RCMs at normal incidence are smaller than 0.2 except one occurrence and only four maximum RCMs are greater than 0.1;
2, a small variation of the medium parameters (the blue dashed and black dotted lines) only slightly influence the trend of the RCMs;
3, for 90° incidence angles, RCMs equal one, which corresponds to total internal reflection;
4, RCMs may have no, one, or two zero RCM point, most RCMs have no zero RCM point.

Additional PSV RCMs properties are:
1, all maximum RCMs are smaller than 0.4 and only four RCMs are greater than 0.2;
2, a small variation of the medium parameters (the blue dashed and black dotted lines) will not dramatically change the trend of the RCMs except cases 2, 5, 9, and 12;
3, for zero and 90° incidence angles, RCMs equal zero;
4, besides zero and 90° incidence angle, most RCMs have one zero RCM point and the others have no zero RCM point;
5, almost all RCMs go as zero $\rightarrow$ local maximum $\rightarrow$ zero or a local minimum $\rightarrow$ local maximum $\rightarrow$ zero.

The common features of all RCMs are:
1, for normal incidence, PP and SH RCMs are relatively small compared with larger offset;
2, most of the RCMs keep relative size between each other after normal incidence to one of the zero RCM points, dramatic change of RCMs' relative size are observed after the first or second zero RCMs;
3, RCMs curve always cross for each variation of medium parameters after the first zero RCMs;

4, gradient discontinuities happen for a lot of large offset RCMs.

Some parameters are more sensitive to RCM in certain angles than Poisson's ratio, which is the main justification for using not only Poisson's ratio. These observations maybe helpful for inversion.

Chapter 3

Seismic Signatures of Pore Connectivity

3.1 Introduction

Anisotropy means direction-dependent physical characteristics, while heterogeneity means position-dependent physical characteristics. One important cause of anisotropy is pores in matrix. The matrix with complex pore structure is heterogeneous, but it can be approximately considered as an equivalently-homogeneous anisotropic medium. This kind of theory is called Effective-Medium Theory (hereafter refer as EMT), which can avoid intensive computations and simplify things significantly.

There are many different kinds of EMT in the literature (Eshelby, 1957; Kuster and Toksöz, 1974; Hudson, 1981; Mavko et al., 2003). One of the exquisite EMT is General Singular Approximation (hereafter refer as GSA). Among the GSA input parameters are pore aspect ratio, crack density, background stiffness-tensor, and inclusion stiffness-tensor. On the other hand, GSA also contains the crucial parameter friability that is thought as controlling the pore space connectivity, which is also the main research object in this chapter. Using GSA to calculate the effective stiffness-tensor was first introduced by Shermergor (1977). The empirical parameter friability was first introduced into GSA in Bayuk and Chesnokov (1998). Tiwary

(2007) and Jiang and Chesnokov (2012) use an isotropic background to model friability variation with the stiffness-tensor and Thomsens parameters. Modeling with a friability value of 0.78 and a background VTI medium was done in Bayuk et al. (2008). Inversion to obtain the value of friability can be found in Bayuk et al. (2007), Bayuk et al. (2008), and Jiang (2013).

However, none of the previous literature simultaneously study the influence of friability variation on stiffness-tensor components, extended Thomsens parameters, phase velocities, critical angles, and PP wave reflection coefficient with a VTI background, especially critical angles and PP reflection coefficients. Here, the critical angles and PP reflection coefficients are calculated between a fractured orthorhombic medium and unfractured VTI medium. The fractured orthorhombic medium can be both gas and water-saturated.

After the calculation through GSA, I get the stiffness-tensor that may include up to 21 different parameters. With density, they approximately include all the information about the subsurface structure. The stiffness-tensor and density can be regarded as input parameters to calculate relevant seismic signatures such as extended Thomsen's parameters, phase velocity, critical angle, and general anisotropic reflection coefficient. Calculating different signatures are important in that different signatures usually have different sensitivity to medium parameters. Understanding this sensitivity is helpful for inversion of GSA input parameters.

I briefly review the theory of GSA firstly. Then I explain the procedure of calculating above mentioned seismic signatures. Lastly, I focus on presenting numerical results, discussions, conclusions, and possible future work about the influence of friability on seismic signatures.

3.2 General singular approximation

In principle, it is hard to say which EMT is the best. The ultimate check of the accuracy of different EMTs should be based on experimental results. In this regard, Rathore et al. (1994) have done an experiment, and the result was modeled by Bayuk and Chesnokov (1998), which shows the more accurate nature of GSA.

In the derivation of GSA, firstly, a comparison body has to be established from inhomogeneous body. Secondly, the differential operator in Newton's law, stiffness-tensor, strain, and displacement are divided into the average and fluctuation parts. Thirdly, using Green's function and dropping the high-order term, the expression of the effective stiffness-tensor is:

$$C^{*} =< C(I - QC^{'})^{-1} >< (I - QC^{'})^{-1} >^{-1} \tag{3.1}$$

C is the stiffness-tensor of the inhomogeneous body, I is the identity matrix, Q is related to second derivative of Green's function, and $C^{'}$ is the fluctuation of stiffness-tensor. Second derivative of Green's function plays an important role in the computation of GSA. It can be divided into two parts, the singular and formal parts, and dropping the formal part will significantly simplify the calculation. The word "approximation" means dropping the formal part (Fokin, 1973; Bayuk and Chesnokov, 1998).

The input parameters for GSA are: pore aspect ratio, crack density (interchangeable with porosity), stiffness-tensor of the matrix, stiffness-tensor of the inclusion, and (optionally) an empirical parameter "friability". The output is the stiffness-tensor of homogeneous anisotropic body. Figure 3.1 shows this relationship. Friability is possibly related to the connectivity of pores. In the static case of GSA, the pore size is not considered. Friability is the empirical parameter intended to explain experimental data (Bayuk and Chesnokov, 1998). It takes account of many

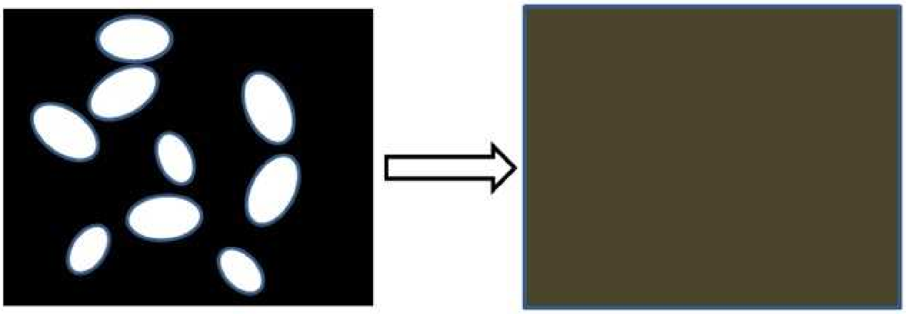

Figure 3.1: An equivalent homogeneous anisotropic rock can represent a heterogeneous porous rock.

factors that can't be rigorously considered. Its range of values is from 0 to 1, with 0 corresponds to pure crystals and 1 corresponds to completely connected pores (Evgeny Chesnokov, personal communication).

In general, the pore aspect ratio is chosen as 0.035 for shale and 0.12 for sandstone (Keys and Xu, 2002). For laboratory data from core, friability can be inverted from velocity measurement assuming the velocity is VTI (Bayuk et al., 2007, 2008; Jiang, 2013). For field data, friability may be regarded as the connected porosity or not considered at all.

3.3 Anisotropy, phase velocity, and polarization

Here I give a brief review of the main governing equations in anisotropy that are used in constructing stiffness-tensor, extended Thomsen's parameters, phase velocity, critical angle, and R/T coefficients in anisotropic medium (Tsvankin, 2005). The meanings of symbols are in Table 3.1. Starting from the second Newton's law without source:

$$\rho \frac{\partial^2 u_i}{\partial t^2} = c_{ijkl} \frac{\partial^2 u_k}{\partial x_j \partial x_l} \tag{3.2}$$

Mathematical symbol	Meaning	
x, y, and z	coordinates	
t	time	
i	$\sqrt{-1}$	
ρ	density	
σ	stress	
ε	strain	
c and C	stiffness-tensor u	displacement
k	wavenumber	
$\|\|$	determinant of a matrix	
θ	azimuthal angle	
φ	incidence angle	
p	wavefront normal	
$\mathbf{d}$	polarization vector	
V	velocity	

Table 3.1: The mathematical symbols and meanings for extended Thomsen's parameters, phase velocities, critical angles, and general anisotropic reflection and transmission coefficients calculation. The units are International System of Units.

due to the symmetry of c_{ijkl}, I have:

$$c_{ijkl}(i,j,k,l=1,2,3) \Rightarrow C_{mn}(m,n=1,2,3,4,5,6)$$

C_{mn} also has symmetry:

$$C_{mn} = \begin{bmatrix} C_{11} & C_{12} & C_{13} & C_{14} & C_{15} & C_{16} \\ & C_{22} & C_{23} & C_{24} & C_{25} & C_{26} \\ & & C_{33} & C_{34} & C_{35} & C_{36} \\ & & & C_{44} & C_{45} & C_{46} \\ & \text{sym} & & & C_{55} & C_{56} \\ & & & & & C_{66} \end{bmatrix}$$

substitute the displacements in plane wave forms into equation 3.2, I have the cubic equation:

$$\left|\Gamma_{ik} - \rho V^2 \delta_{ik}\right| = 0 \Rightarrow \left(\rho V^2\right)^3 + I_1\left(\rho V^2\right)^2 + I_2\left(\rho V^2\right) + I_3 = 0 \tag{3.3}$$

in which:

$$\begin{cases} I_1 = -\Gamma_{ii} \\ I_2 = \frac{1}{2}\left(\Gamma_{ii}\Gamma_{jj} - \Gamma_{ij}\Gamma_{ij}\right) \\ I_3 = -\left|\Gamma_{ij}\right| = -\varepsilon_{ijk}\Gamma_{i1}\Gamma_{j2}\Gamma_{k3} \end{cases}$$

equation 3.3 is essentially the equation:

$$ax^3 + bx^2 + cx + d = 0 (a \neq 0) \tag{3.4}$$

equation 3.4 can be solved by Cardano's method for the phase velocities that are useful for computing critical angle and reflection coefficient (Beyer, 1991), the solutions are:

$$
\begin{cases}
x_1 = \sqrt[3]{-\frac{q}{2} + \sqrt{(\frac{q}{2})^2 + (\frac{p}{3})^3}} + \sqrt[3]{-\frac{q}{2} - \sqrt{(\frac{q}{2})^2 + (\frac{p}{3})^3}} - \frac{b}{3a} \\
x_2 = \omega \sqrt[3]{-\frac{q}{2} + \sqrt{(\frac{q}{2})^2 + (\frac{p}{3})^3}} + \omega^2 \sqrt[3]{-\frac{q}{2} - \sqrt{(\frac{q}{2})^2 + (\frac{p}{3})^3}} - \frac{b}{3a} \\
x_3 = \omega^2 \sqrt[3]{-\frac{q}{2} + \sqrt{(\frac{q}{2})^2 + (\frac{p}{3})^3}} + \omega \sqrt[3]{-\frac{q}{2} - \sqrt{(\frac{q}{2})^2 + (\frac{p}{3})^3}} - \frac{b}{3a}
\end{cases}
$$

in which: $\omega = -\frac{1}{2} + \frac{\sqrt{3}}{2}i$, $p = c - \frac{b^2}{3a}$, and $q = \frac{2b^3}{27a^2} - \frac{bc}{3a} + d$. The polarization vector $\mathbf{d}$ equals (d_1, d_2, d_3), which is useful for calculating R/T coefficient. Polarization vector can be computed from algebraic manipulations of the left side of equation 3.3:

$$\frac{d_1}{\Gamma_{13}(\Gamma_{22} - \rho V^2) - \Gamma_{12}\Gamma_{23}} = \frac{d_2}{(\Gamma_{11} - \rho V^2)\Gamma_{23} - \Gamma_{12}\Gamma_{13}} = \frac{d_3}{\Gamma_{12}\Gamma_{12} - (\Gamma_{11} - \rho V^2)(\Gamma_{22} - \rho V^2)} \tag{3.5}$$

which has to satisfy the normalization condition:

$$d_1^2 + d_2^2 + d_3^2 = 1$$

3.3.1 Orthorhombic anisotropy

In the main part of this section, I reviewed the basic equation for anisotropy that is up to triclinic, which has 21 independent elastic parameters. Nevertheless, triclinic anisotropy is of only limited interested in current exploration geophysics context. The three most popular anisotropic symmetries are VTI, HTI, and orthorhombic anisotropy that contains five, five, and nine independent parameters, respectively.

Crystal symmetry is one cause of anisotropy. In current anisotropic seismic exploration context, beside crystal symmetry, the other main causes of VTI anisotropy are horizontal layering, overburden stress, horizontal fracture; the main cause of HTI anisotropy is vertical fracture. When the cause of VTI and HTI anisotropy coexist in a medium, the result is orthorhombic anisotropy. Orthorhombic anisotropy can also be caused by non-circular cracks, crack plane misalignment, and multiple crack systems in an isotropic background (Tsvankin, 1997a).

Since a GSA-based description of fracture parameters in terms of orthorhombic anisotropy is very limited, this chapter focuses on orthorhombic anisotropy caused by a background VTI medium with vertical fractures. A background VTI medium has five independent parameters, the GSA modeling has another at least four independent parameters (friability, aspect ratio, crack density, and inclusion stiffness-tensor component), so the calculated medium has at least nine independent parameters. This is different from the linear slip theory in which two of the nine parameters are related.

Vertical fractures can be found in some shale such as Barnett shale that is tilted more than 75° (Tiwary, 2007). Recently, the seismic imaging community has found orthorhombic anisotropy is helpful for flattening their gathers and structural imaging (Li et al., 2012, 2013). However, besides theoretical analysis, numerical modeling, and physical modeling, practical extraction and application of the orthorhombic anisotropy is still not very popular. A condensed matrix notation of orthorhombic anisotropy is:

$$\begin{bmatrix} C_{11} & C_{12} & C_{13} & 0 & 0 & 0 \\ & C_{22} & C_{23} & 0 & 0 & 0 \\ & & C_{33} & 0 & 0 & 0 \\ & & & C_{44} & 0 & 0 \\ & sym & & & C_{55} & 0 \\ & & & & & C_{66} \end{bmatrix}$$

A schematic diagram of orthorhombic medium inserted by vertical fracture in a VTI background can be found in the upper layer of Figure 3.2.

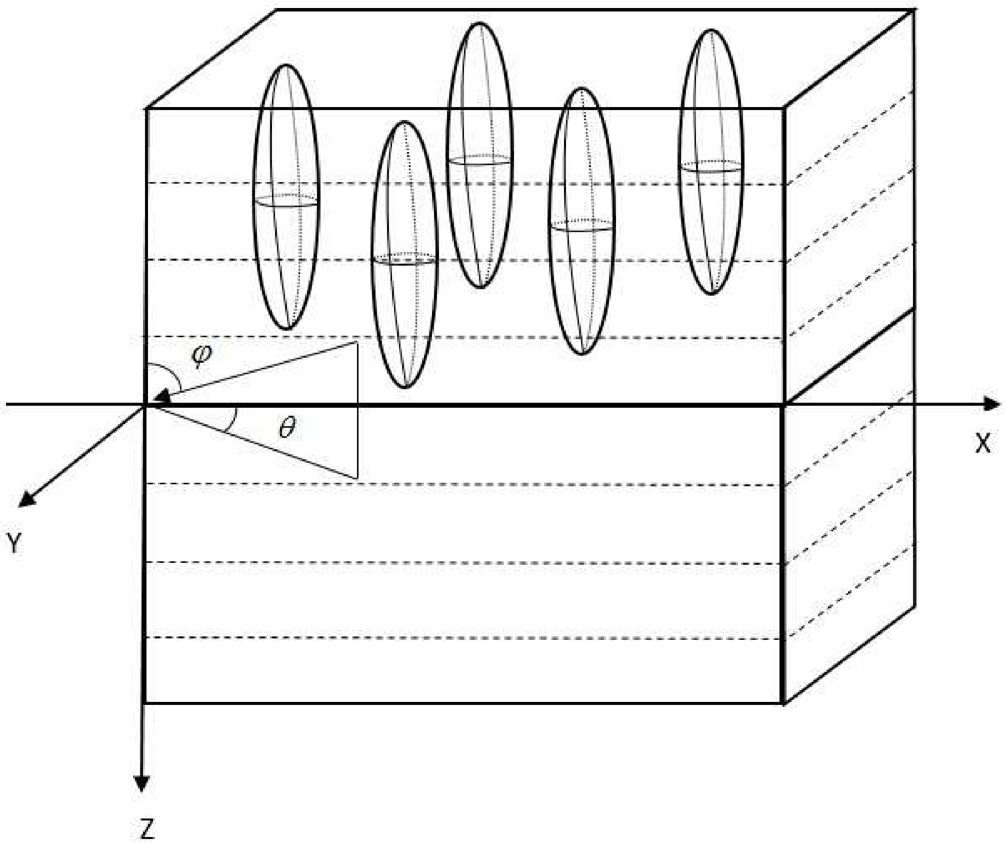

Figure 3.2: PP wave incident between orthorhombic and VTI media. Upper layer has orthorhombic anisotropy caused by background horizontal layering and aligned ellipsoid; lower layer has background VTI anisotropy only that is caused by horizontal layering. The upper and lower layers have the same background VTI anisotropy. φ is the incidence angle that is measured from the Z axis and θ is the azimuth angle that is measured from the Y axis.

3.4 General anisotropic reflection and transmission coefficients

Due to the presence of strong anisotropy in the orthorhombic model, the weak anisotropic reflection approximate formulas (Rüger, 1998; Vavrycuk and Psencik, 1998) are not applicable. In following, I show the procedure of calculating the exact R/T coefficients.

General anisotropic R/T problem is an extension of Zoeppritz equation. The incidence and generation of waves from R/T in anisotropic media are schematically shown in Figure 3.3. Several literature describe the exact general anisotropic R/T coefficients (Keith and Crampin, 1977; Schoenberg and Protazio, 1992; Chen, 2000; Chattopadhyay, 2006). Although Schoenberg's approach is more compact, I slightly modify and use the approach of Chattopadhyay (2006) here due to its simplicity. Also, the Schoenberg method can only deal with monoclinic or higher symmetry, while my approach can deal with arbitrary anisotropic medium. The difference between my approach and Chattopadhyay (2006) approach is that Chattopadhyay (2006) formulates the matching of stress and strain in a specific symmetry plane, my approach doesn't need to specify a symmetry plane. It follows that my approach can be checked if the calculated results are rotated into certain symmetry plane that has higher symmetry.

The displacements in anisotropic medium can be written as:

$$\begin{pmatrix} u_x^n \\ \\ u_y^n \\ \\ u_z^n \end{pmatrix} = A_n \begin{pmatrix} d_1^n \\ \\ d_2^n \\ \\ d_3^n \end{pmatrix} e^{ik_n(x_1 p_1^n + x_2 p_2^n + x_3 p_3^n - c_n t)}$$

In this equation, the meanings of symbols are summarized in Table 3.1. It is assumed the incident wave amplitude is 1. Reflected P, reflected S_1, reflected S_2, transmitted P, transmitted S_1, and transmitted S_2 waves are represented by n of 1, 2, 3, 4, 5, and 6, respectively. A schematic diagram of the reflection formulation is shown in Figure 3.3.

Wavefront normals are related to incidence and azimuthal angle as:

$$\text{incident wave}: p_{1\text{in}} = -\sin\varphi_{\text{in}}\sin\theta,\ p_{2\text{in}} = -\sin\varphi_{\text{in}}\cos\theta,\ \text{and}\ p_{3\text{in}} = \cos\varphi_{\text{in}}$$

$$\text{reflected wave}: p_{1\text{rf}} = -\sin\varphi_{\text{rf}}\sin\theta,\ p_{2\text{rf}} = -\sin\varphi_{\text{rf}}\cos\theta,\ \text{and}\ p_{3\text{rf}} = -\cos\varphi_{\text{rf}}$$

$$\text{transmitted wave}: p_{1\text{tr}} = -\sin\varphi_{\text{tr}}\sin\theta,\ p_{2\text{tr}} = -\sin\varphi_{\text{tr}}\cos\theta,\ \text{and}\ p_{3\text{tr}} = \cos\varphi_{\text{tr}}$$

Snell's law means horizontal phase slowness is constant across layers. A numerical method is needed for application of Snell's law when anisotropy lower than VTI is present, for which I choose the bisection method.

Three displacements and three stress boundary conditions are needed for calculating the six reflected and transmitted wave amplitudes:

$$u_x^I = u_x^0 + u_x^1 + u_x^2 + u_x^3 = u_x^4 + u_x^5 + u_x^6 = u_x^{II}$$

$$u_y^I = u_y^0 + u_y^1 + u_y^2 + u_y^3 = u_y^4 + u_y^5 + u_y^6 = u_y^{II}$$

$$u_z^I = u_z^0 + u_z^1 + u_z^2 + u_z^3 = u_z^4 + u_z^5 + u_z^6 = u_z^{II}$$

$$\sigma_{xz}^I = \sigma_{xz}^0 + \sigma_{xz}^1 + \sigma_{xz}^2 + \sigma_{xz}^3 = \sigma_{xz}^4 + \sigma_{xz}^5 + \sigma_{xz}^6 = \sigma_{xz}^{II}$$

$$\sigma_{yz}^I = \sigma_{yz}^0 + \sigma_{yz}^1 + \sigma_{yz}^2 + \sigma_{yz}^3 = \sigma_{yz}^4 + \sigma_{yz}^5 + \sigma_{yz}^6 = \sigma_{yz}^{II}$$

$$\sigma_{zz}^I = \sigma_{zz}^0 + \sigma_{zz}^1 + \sigma_{zz}^2 + \sigma_{zz}^3 = \sigma_{zz}^4 + \sigma_{zz}^5 + \sigma_{zz}^6 = \sigma_{zz}^{II}$$

The Hooke's law that relates stress and strain can be expanded as:

$$\begin{aligned}
\sigma_{xz} &= c_{13kl}\varepsilon_{kl} = ik_n A_n e^{ik_n(x_1 p_1^n + x_2 p_2^n + x_3 p_3^n - c_n t)} P_n \\
\sigma_{yz} &= c_{23kl}\varepsilon_{kl} = ik_n A_n e^{ik_n(x_1 p_1^n + x_2 p_2^n + x_3 p_3^n - c_n t)} Q_n \\
\sigma_{zz} &= c_{33kl}\varepsilon_{kl} = ik_n A_n e^{ik_n(x_1 p_1^n + x_2 p_2^n + x_3 p_3^n - c_n t)} R_n
\end{aligned} \tag{3.6}$$

in which:

$$P_n = C_{51}p_1^n d_1^n + C_{52}p_2^n d_2^n + C_{53}p_3^n d_3^n + C_{54}(p_3^n d_2^n + p_2^n d_3^n) +$$

$$C_{55}(p_3^n d_1^n + p_1^n d_3^n) + C_{56}(p_2^n d_1^n + p_1^n d_2^n)$$

$$Q_n = C_{41}p_1^n d_1^n + C_{42}p_2^n d_2^n + C_{43}p_3^n d_3^n + C_{44}(p_3^n d_2^n + p_2^n d_3^n) +$$

$$C_{45}(p_3^n d_1^n + p_1^n d_3^n) + C_{46}(p_2^n d_1^n + p_1^n d_2^n)$$

$$R_n = C_{31}p_1^n d_1^n + C_{32}p_2^n d_2^n + C_{33}p_3^n d_3^n + C_{34}(p_3^n d_2^n + p_2^n d_3^n) +$$

$$C_{35}(p_3^n d_1^n + p_1^n d_3^n) + C_{36}(p_2^n d_1^n + p_1^n d_2^n)$$

The velocities in equation 3.6 are phase velocities.

After some manipulations, I get:

$$\begin{pmatrix}
\frac{d_1^1}{d_1^0} & \frac{d_1^2}{d_1^0} & \frac{d_1^3}{d_1^0} & -\frac{d_1^4}{d_1^0} & -\frac{d_1^5}{d_1^0} & -\frac{d_1^6}{d_1^0} \\
\frac{d_2^1}{d_2^0} & \frac{d_2^2}{d_2^0} & \frac{d_2^3}{d_2^0} & -\frac{d_2^4}{d_2^0} & -\frac{d_2^5}{d_2^0} & -\frac{d_2^6}{d_2^0} \\
\frac{d_3^1}{d_3^0} & \frac{d_3^2}{d_3^0} & \frac{d_3^3}{d_3^0} & -\frac{d_3^4}{d_3^0} & -\frac{d_3^5}{d_3^0} & -\frac{d_3^6}{d_3^0} \\
\frac{P_1 k_1}{P_0 k_0} & \frac{P_2 k_2}{P_0 k_0} & \frac{P_3 k_3}{P_0 k_0} & -\frac{P_4 k_4}{P_0 k_0} & -\frac{P_5 k_5}{P_0 k_0} & -\frac{P_6 k_6}{P_0 k_0} \\
\frac{Q_1 k_1}{Q_0 k_0} & \frac{Q_2 k_2}{Q_0 k_0} & \frac{Q_3 k_3}{Q_0 k_0} & -\frac{Q_4 k_4}{Q_0 k_0} & -\frac{Q_5 k_5}{Q_0 k_0} & -\frac{Q_6 k_6}{Q_0 k_0} \\
\frac{R_1 k_1}{R_0 k_0} & \frac{R_2 k_2}{R_0 k_0} & \frac{R_3 k_3}{R_0 k_0} & -\frac{R_4 k_4}{R_0 k_0} & -\frac{R_5 k_5}{R_0 k_0} & -\frac{R_6 k_6}{R_0 k_0}
\end{pmatrix}
\begin{pmatrix} A_1 \\ A_2 \\ A_3 \\ A_4 \\ A_5 \\ A_6 \end{pmatrix}
=
\begin{pmatrix} -1 \\ -1 \\ -1 \\ -1 \\ -1 \\ -1 \end{pmatrix} \tag{3.7}$$

In equation 3.7, A_1, A_2, A_3, A_4, A_5, and A_6 correspond to the displacement amplitudes of reflected or transmitted P or S waves. Solving these equations, I can get

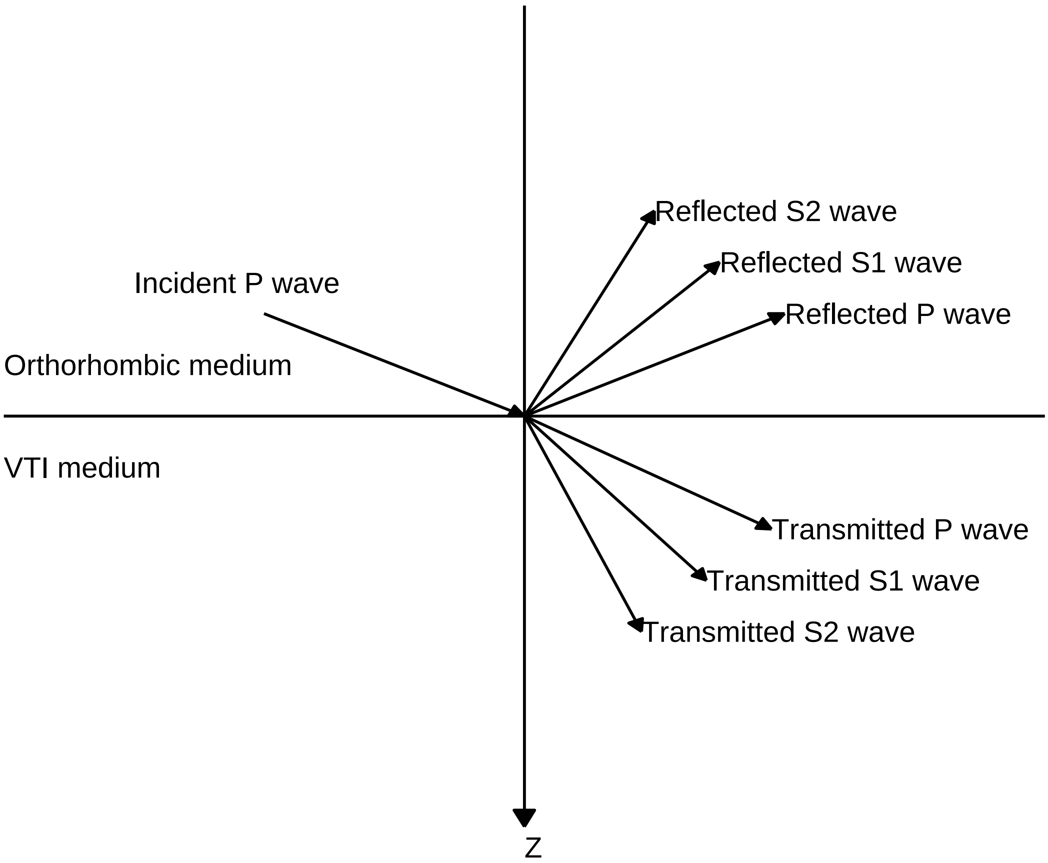

Figure 3.3: P wave reflection between an orthorhombic medium and a VTI medium has three reflected and transmitted waves. This corresponds to the incident plane at Figure 3.2.

the R/T coefficients for general anisotropic media.

3.5 Numerical results

3.5.1 General singular approximation

Example 1

In this example, I choose the parameters of Rathore et al. (1994) and Mavko et al. (2003) as input for calculating effective stiffness-tensor. The cracks are ellipsoids, the ratio of crack thickness to crack diameter is $0.02/5.5 = 0.003636$ which means the crack is flat with equally long X and Y axes. The crack density is 0.01; friability is chosen such that $C^c = 0.5C^m + 0.5C^f$. C^c is the stiffness-tensor of the comparison body, C^m is the stiffness-tensor of the matrix, and C^f is the stiffness-tensor of the inclusion fluid. The matrix is isotropic sandstone (Rathore et al., 1994):

$$\begin{bmatrix} 33.5333 & 8.133 & 8.133 & 0 & 0 & 0 \\ & 33.5333 & 8.133 & 0 & 0 & 0 \\ & & 33.5333 & 0 & 0 & 0 \\ & & & 12.7 & 0 & 0 \\ & \text{sym} & & & 12.7 & 0 \\ & & & & & 12.7 \end{bmatrix}$$

The inclusion is isotropic water with salinity 50000 ppm and bulk modulus 3.013 GPa (Mavko et al., 2003). The output stiffness-tensor is vertically transversely isotropic:

$$\begin{bmatrix} 32.9661 & 7.9720 & 7.5275 & 0 & 0 & 0 \\ & 32.9661 & 7.5275 & 0 & 0 & 0 \\ & & 29.5397 & 0 & 0 & 0 \\ & & & 8.5350 & 0 & 0 \\ & \text{sym} & & & 8.5350 & 0 \\ & & & & & 12.4971 \end{bmatrix}$$

Example 2

This example generates an HTI medium with the symmetry axis along the X direction. Other parameters are the same as previous section except the shape of the crack with regard to the coordinate system. This time the crack is short along the X axis but equally long along the Y and Z axis. The output stiffness-tensor is horizontally transversely isotropic:

$$\begin{bmatrix} 29.5397 & 7.5275 & 7.5275 & 0 & 0 & 0 \\ & 32.9661 & 7.9720 & 0 & 0 & 0 \\ & & 32.9661 & 0 & 0 & 0 \\ & & & 12.4971 & 0 & 0 \\ & \text{sym} & & & 8.5350 & 0 \\ & & & & & 8.5350 \end{bmatrix}$$

In example 1, because the ellipsoid has equally long axis at X and Y directions, but short axis at Z direction, the modelled medium is VTI, which agrees with

Table 3.2: Stiffness-tensor and density of the VTI background shale. The stiffness-tensor unit is GPa and density unit is g/cm^3

C_{11}	C_{13}	C_{33}	C_{44}	C_{66}	Density
34.3	10.7	22.7	5.4	10.6	2.3

our intuition. Similar input values that generate HTI medium from an isotropic background medium also agrees with our intuition. These validate the code.

3.5.2 Friability variation with stiffness-tensor components

Stiffness-tensor directly relates stress and strain through Hooke's law. Extended Thomsen's parameters, phase velocity, critical angle, and reflection coefficient are all based on stiffness-tensor. In consequence, I calculate stiffness-tensor components variation with friability first. The stiffness-tensor and density of the background VTI medium is from Jones and Wang (1981), which is listed in Table 3.2. The crack density of the fracture is 0.1, which is a popular number in many seismic exploration literature; the aspect ratio is 0.035, which is from Keys and Xu (2002) for shale. The friability changes from 0 to 0.99 with 0.05 increment. This example is used as input for following calculations.

Since porosity and density don't change, the square root of stiffness-tensor component is exactly proportional to the corresponding velocity if the velocity is determined by a single stiffness-tensor component. This happens at the symmetry axis.

Figure 3.4 and 3.5 show the results of stiffness-tensor components variation with friability of the gas and water-saturated orthorhombic media. As friability increases, most stiffness-tensor components decrease in both media, the three stiffness-tensor components that increase are C_{12}, C_{13}, and C_{23} in water-saturated medium. C_{44} in gas-saturated medium almost entirely equals water-saturated medium until friability increases up to 0.6. The two very large decreases are: C_{11} in gas-saturated medium, which corresponds to decrease of horizontal gas-saturated P wave velocity along the X axis; C_{55} and C_{66} in both media. C_{55} corresponds to SV wave phase velocity along the X and Z axis and C_{66} corresponds to SH wave phase velocity along the X and Y axes. C_{44}, C_{55}, and C_{66} are mostly responsible for shear wave velocity, thus they are almost the same for gas and water-saturated media. In Gassmann's theory, they are exactly same, which means saturated shear modulus is independent of fluid modulus. In my analysis, they are a little bit different with different fluid saturation, this is believed to be GSA modeling considers the different kind of interaction between the two phases.

3.5.3 Friability variation with extended Thomsen's parameters

Thomsen's parameters are the mainstream and more useful representation of the stiffness-tensor. For VTI medium, it recasts the stiffness-tensor into another five parameters: vertical P wave velocity, vertical S wave velocity, γ, ϵ, and δ. γ basically measures the percentage of horizontal SH wave phase velocity deviation from the vertical direction, ϵ basically means the percentage of horizontal P wave phase velocity deviation from the vertical direction, and δ means the phase velocity curvature at normal incidence. δ is also close to the percentage difference between P wave moveout and vertical velocity (Thomsen, 1986; Tsvankin, 1997b, 2005). Thomsen's parameters also have many other meanings.

Orthorhombic medium has three symmetry planes. In each of the symmetry plane, the medium shows transversely isotropic characteristics if two special parameters are equal. Thus Tsvankin (1997a) extends the concept of Thomsen (1986) into

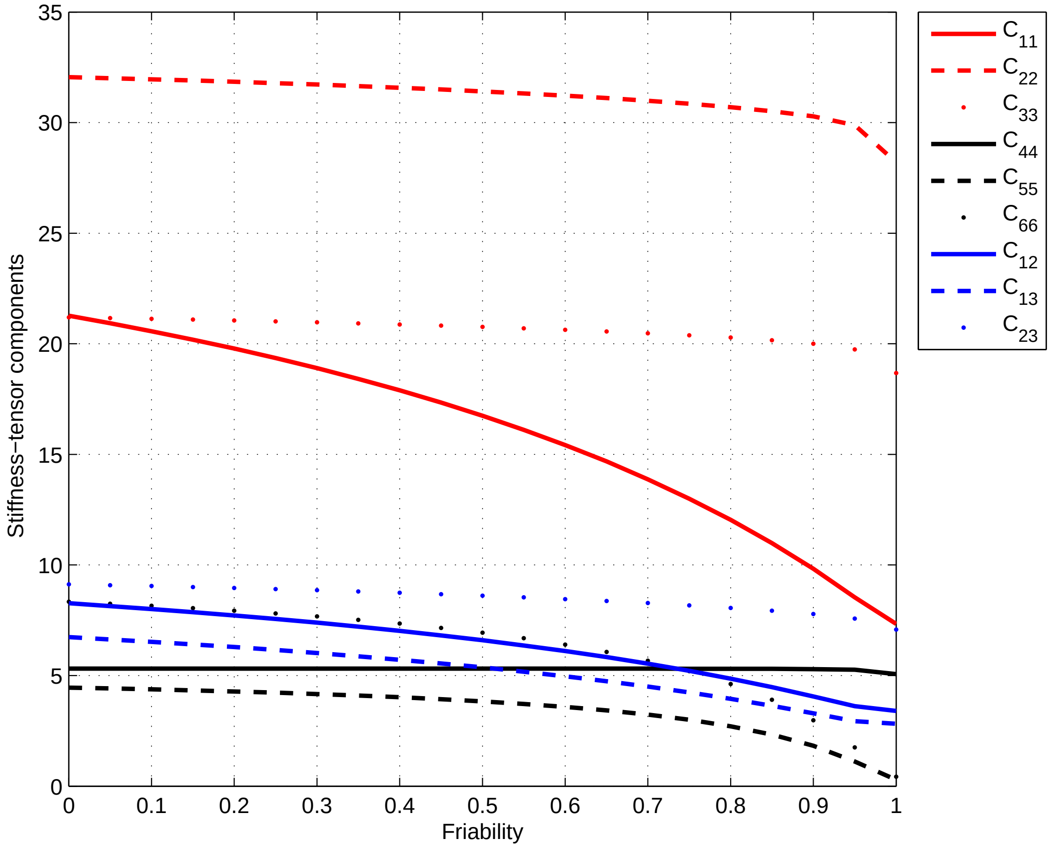

Figure 3.4: Stiffness-tensor components variation with friability in the gas-saturated orthorhombic medium. Background stiffness-tensor and density are listed in Table 3.2. The crack density is 0.1, aspect ratio is 0.035, and the friability changes from 0 to 0.99 with 0.05 increment.

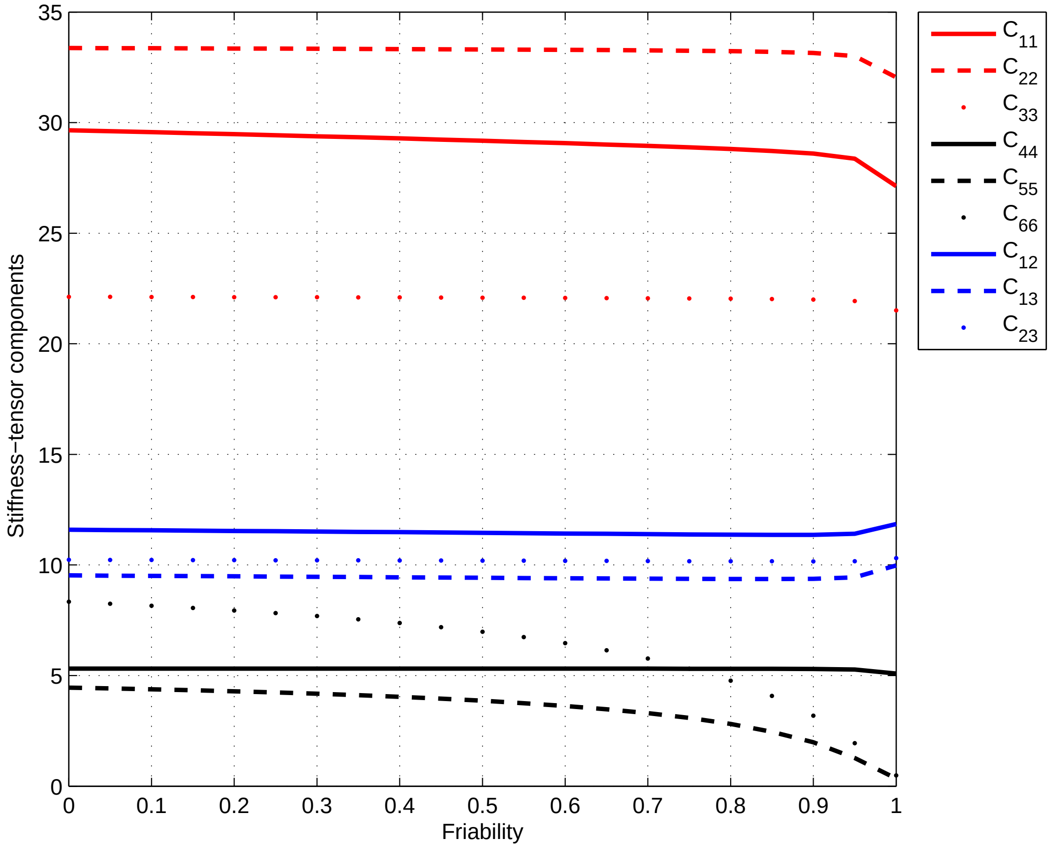

Figure 3.5: Stiffness-tensor components variation with friability in the water-saturated orthorhombic medium. Background stiffness-tensor and density are listed in Table 3.2. The crack density is 0.1, aspect ratio is 0.035, and the friability changes from 0 to 0.99 with 0.05 increment.

orthorhombic medium, which needs vertical P and S wave velocities and following seven parameters to fully characterize orthorhombic medium:

$$\varepsilon^1 = \frac{C_{22}-C_{33}}{2C_{33}}$$

$$\varepsilon^2 = \frac{C_{11}-C_{33}}{2C_{33}}$$

$$\gamma^1 = \frac{C_{66}-C_{55}}{2C_{55}}$$

$$\gamma^2 = \frac{C_{66}-C_{44}}{2C_{44}}$$

$$\delta^1 = \frac{(C_{23}+C_{44})^2-(C_{33}-C_{44})^2}{2c_{33}(C_{33}-C_{44})}$$

$$\delta^2 = \frac{(C_{13}+C_{55})^2-(C_{33}-C_{55})^2}{2C_{33}(C_{33}-C_{55})}$$

$$\delta^3 = \frac{(C_{12}+C_{66})^2-(C_{11}-C_{66})^2}{2C_{11}(C_{11}-C_{66})}$$

The superscripts correspond to different symmetry plane: 1 represents the plane YZ, 2 represents the plane XZ, and 3 represents the plane XY. Computed results of extended Thomsen's parameters are displayed in Figure 3.6 and 3.7. The value weak anisotropy in Thomsen (1986) means it is less than 0.2. As can be seen from these figures, in both media the anisotropy parameters are larger than 0.2 for lots of occurrences. Consequently, weak anisotropic approximations are not applicable in my case.

These two figures tell us not all extended Thomsen's parameters are sensitive to friability. ϵ^2, γ^2, δ^2, and δ^3 in gas-saturated medium and ϵ^1, δ^2, and δ^3 in water-saturated medium are particular sensitive to friability. Most extended decreases; ϵ^1 increases until friability equals 0.95 and then decreases; δ^1 decreases until friability equals 0.95, at which point it then decreases; ϵ^1 increases until friability equals 0.95 and then decreases; δ^1 decreases until friability equals 0.95, at which point it increases. In water-saturated medium, the exception is δ^1 first decreases slightly and then increases dramatically in the intermediate range of friability.

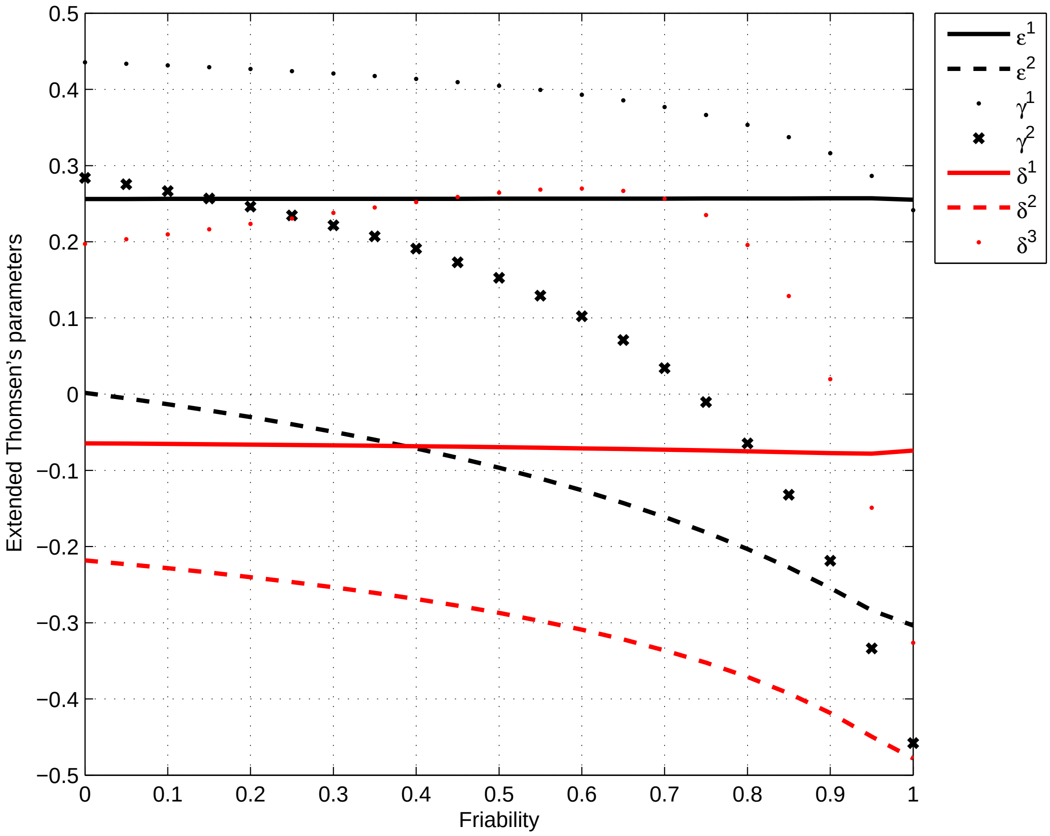

Figure 3.6: Extended Thomsen's parameters variation with friability in gas-saturated orthorhombic medium. Background stiffness-tensor and density are listed in Table 3.2. The crack density is 0.1, aspect ratio is 0.035, and the friability changes from 0 to 0.99 with 0.05 increment.

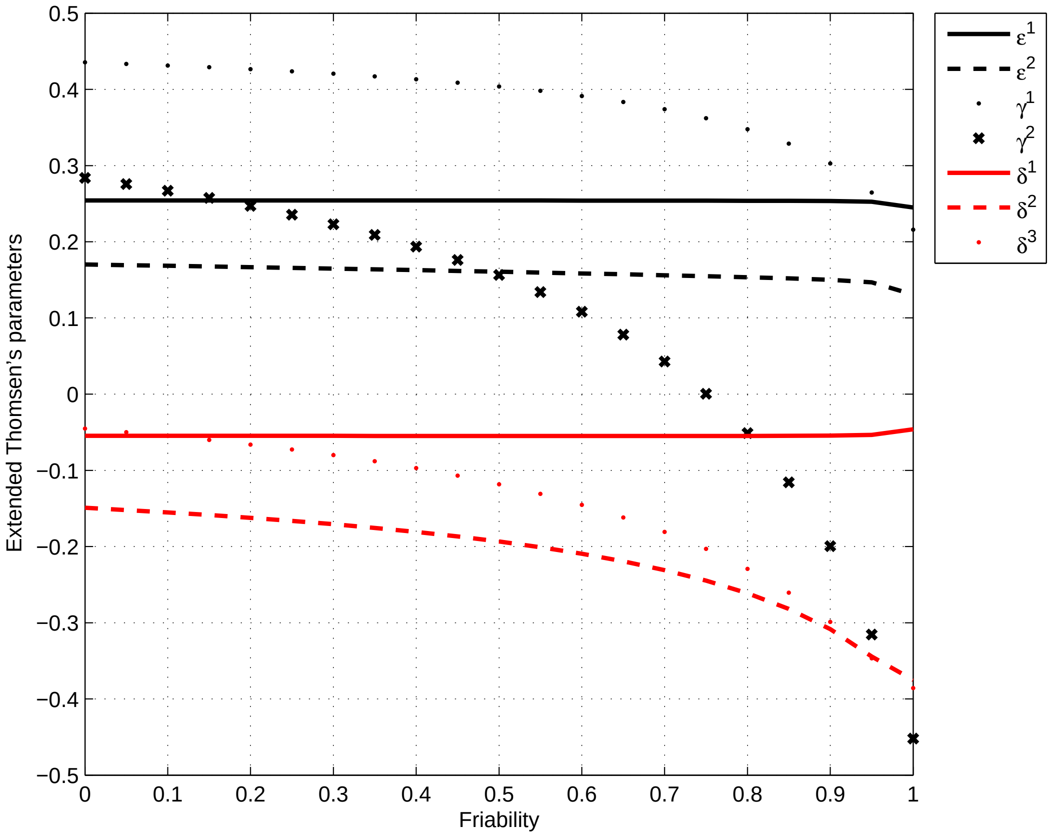

Figure 3.7: Extended Thomsen's parameters variation with friability in water-saturated orthorhombic medium. Background stiffness-tensor and density are listed in Table 3.2. The crack density is 0.1, aspect ratio is 0.035, and the friability changes from 0 to 0.99 with 0.05 increment.

3.5.4 Friability variation with phase velocities

While the analysis of stiffness-tensor and extended Thomsen's parameters are helpful for understanding friability's influence on orthorhombic medium characteristics, they mostly focus on the properties at the symmetry axis or their fractional difference. Out of the symmetry plane characteristics are also important for the following critical angle and azimuthal AVO analysis. The asymptotic formulas to describe phase velocity out of the symmetry plane are complicated, and not easily or well appreciated (Sayers, 1994; Tsvankin, 1997a). At the same time, the characteristics of orthorhombic medium is conspicuously revealed by plotting the exact phase velocities of the three waves out of the symmetry plane. Here, I plot the 3D surfaces of phase velocities variations with the friability equals 0, 0.2, 0.4, 0.6, 0.8, and 0.99.

Figure 3.8, 3.9, 3.10, 3.11, 3.12, and 3.13 show the phase velocities variation with friability of P, S_1, and S_2 waves in gas-saturated medium and P, S_1, and S_2 waves in water-saturated medium, respectively. Only one quadrant's velocity is plotted since it can represent all the other seven quadrants in triclinic medium.

If an orthorhombic medium is only slightly deviated from VTI, plotted phase velocity surface is still close to azimuthally invariant. In this case, we can name the Z axis as the quasi vertical symmetry axis. Similarly, we can name the X and Y axes as the quasi horizontal symmetry axis of the orthorhombic medium if the medium is not far from HTI.

Several observations can be made about these results. Overall, these plots reveal that only using stiffness-tensor and extended Thomsen's parameters to describe the medium will miss majority of the information content. When friability is small (f=0, 0.2, or 0.4), P and S_1 waves have quasi vertical symmetry axis for both gas and water-saturated media. Large friability (f=0.99) distorts this observation that makes the quasi vertical symmetry axis disappears and both gas and water-saturated media have quasi horizontal symmetry axis. This means the media are close to HTI symmetry with an X and/or Y symmetry axis instead of VTI symmetry. For the S_2 wave in both media, phase velocity surfaces show large variations and little transverse isotropy.

Since stiffness-tensor components generally decrease as friability increases, and the density is constant, maximum phase velocities all correspond to friability equals zero and minimum phase velocities all correspond to friability equals 0.99 for both media. The modeled results show sophisticated relationship between phase velocity and friability out of the symmetry plane, especially for S_2 wave. P wave phase velocity maxima in each subplot is close to Y axis for both media; while for S_1 and S_2 waves phase velocity surfaces, velocity maxima may far from any symmetry axis. Velocity minima is more random than maxima.

3.5.5 Friability variation with critical angles

Critical angle is the angle of the incident wave that makes the transmitted wave has 90° transmission angle, which corresponds to horizontal velocity in the lower layer. Since the lower layer is VTI here, Snell's law can be written as:

$$\frac{\sin\varphi}{V_1(\varphi,\theta)} = \frac{1}{V_2^{horizontal}} = \sqrt{\frac{\rho_2}{C_{11\_2}}} \tag{3.8}$$

As Figure 3.2 shows, φ is the angle between vertical axis and incident P wave, θ is the azimuth angle count from X axis, ρ_2 is the density of lower medium, and C_{11_2} is the 11 component of lower medium stiffness-tensor. $V_2^{horizontal}$ is azimuthally invariant, yet $V_1(\varphi,\theta)$ is azimuthally dependent, I need to first determine the azimuth angle, then numerically solve for the critical angle φ from equation 3.8.

The first recognition of critical angle effect on seismic data was at 50s of 20th century (Winterstein and Hanten, 1985). In Winterstein and Hanten (1985), the authors show obvious P and SH waves supercritical reflections. Recently, critical

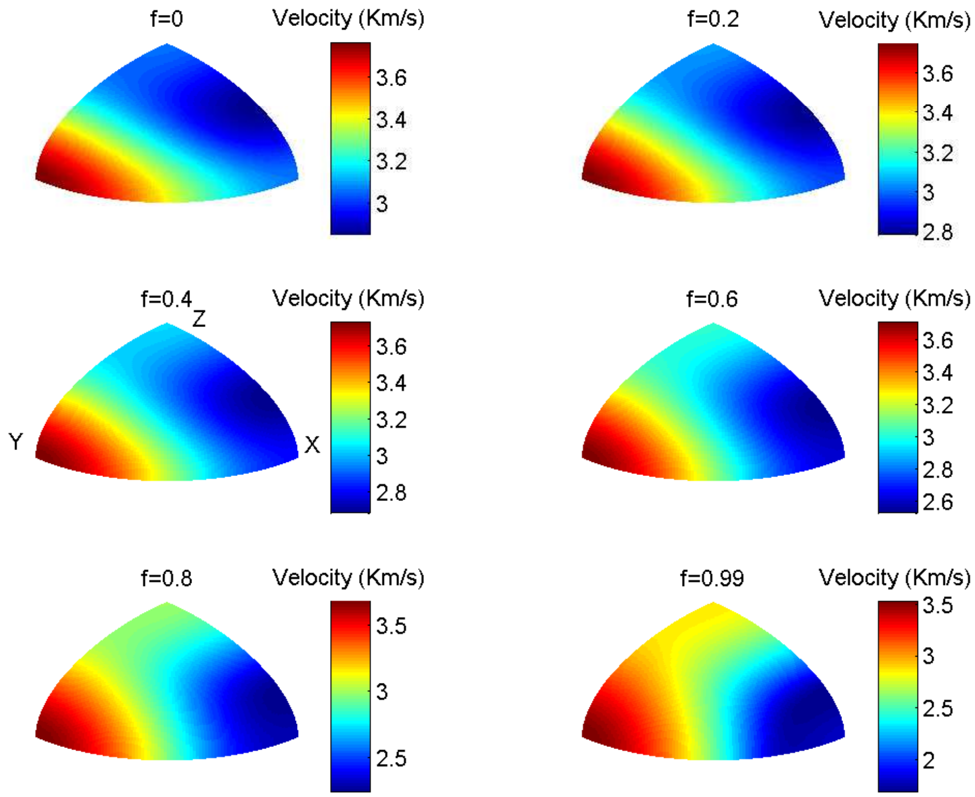

Figure 3.8: P wave phase velocities variation with friability in gas-saturated fractured orthorhombic medium. Background stiffness-tensor and density are listed in Table 3.2. The crack density is 0.1, aspect ratio is 0.035, and the friability changes from 0 to 0.99 with 0.2 increment.

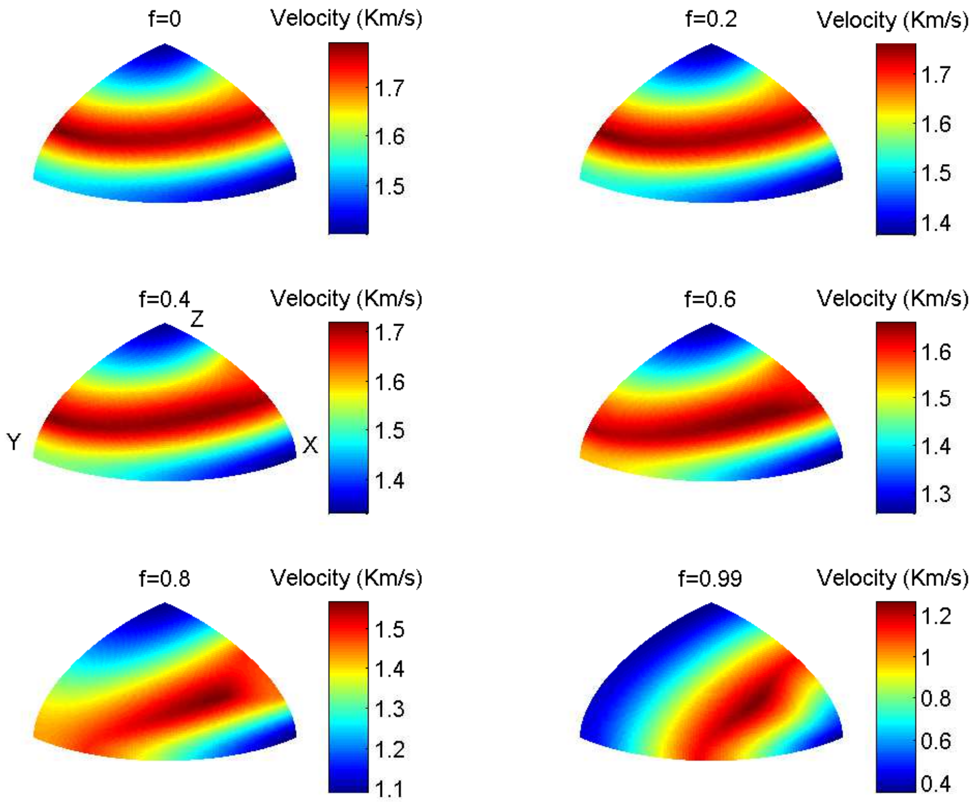

Figure 3.9: S_1 wave phase velocities variation with friability in gas-saturated fractured orthorhombic medium. Background stiffness-tensor and density are listed in Table 3.2. The crack density is 0.1, aspect ratio is 0.035, and the friability changes from 0 to 0.99 with 0.2 increment.

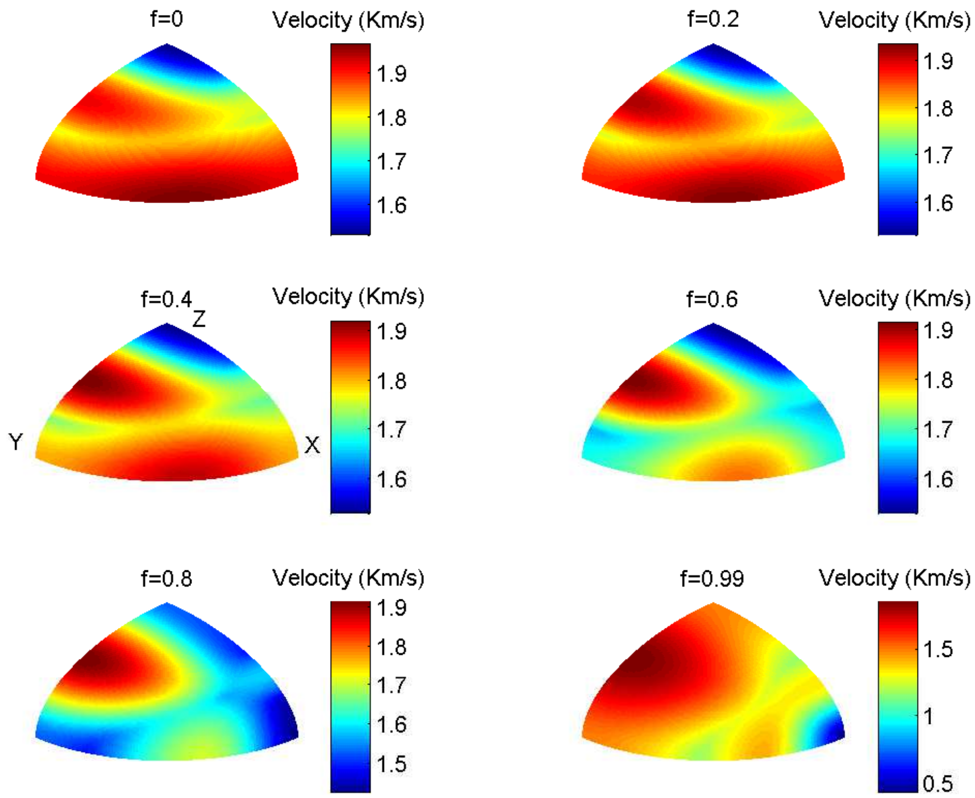

Figure 3.10: S_2 wave phase velocities variation with friability in gas-saturated fractured orthorhombic medium. Background stiffness-tensor and density are listed in Table 3.2. The crack density is 0.1, aspect ratio is 0.035, and the friability changes from 0 to 0.99 with 0.2 increment.

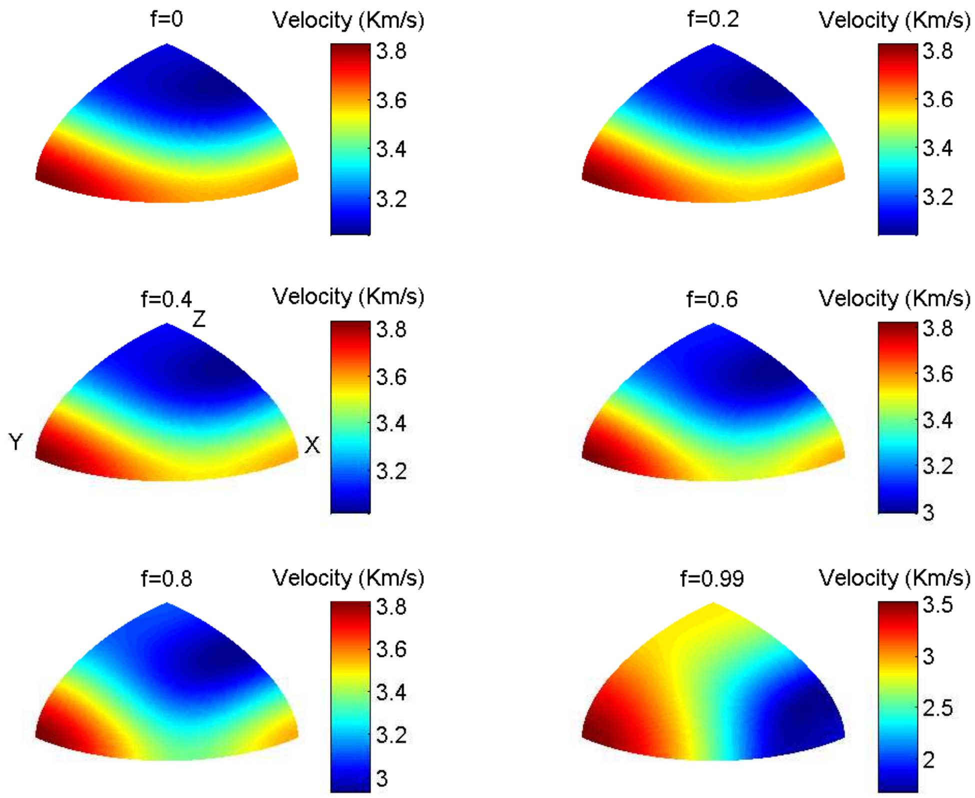

Figure 3.11: P wave phase velocities variation with friability in water-saturated fractured orthorhombic medium. Background stiffness-tensor and density are listed in Table 3.2. The crack density is 0.1, aspect ratio is 0.035, and the friability changes from 0 to 0.99 with 0.2 increment.

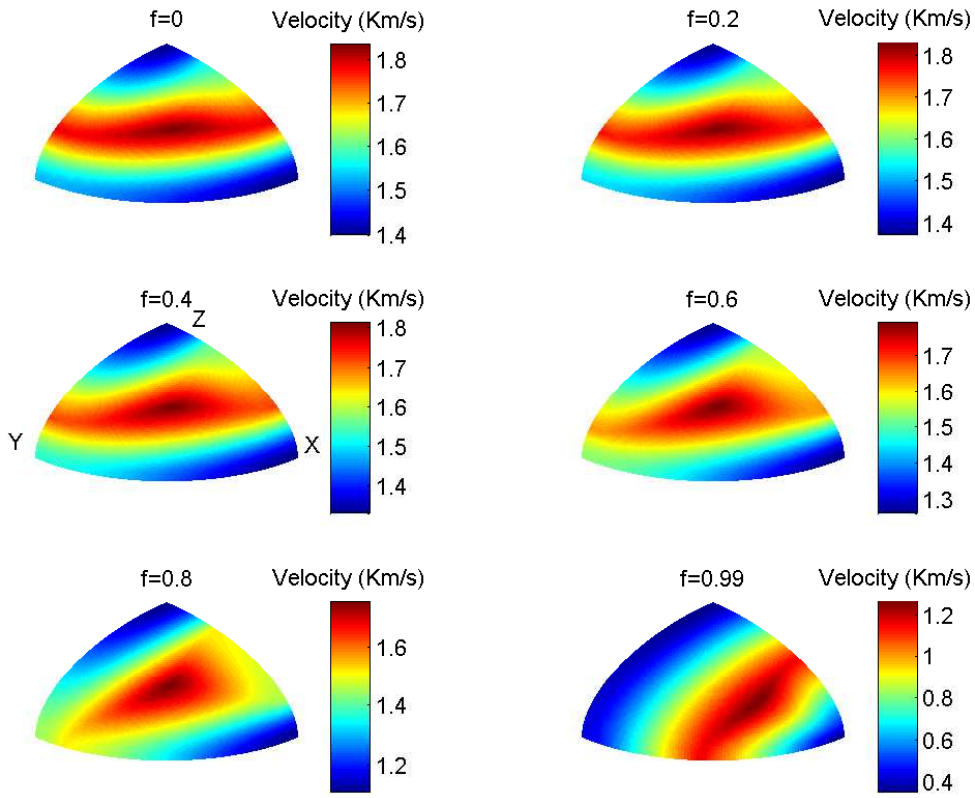

Figure 3.12: S_1 wave phase velocities variation with friability in water-saturated fractured orthorhombic medium. Background stiffness-tensor and density are listed in Table 3.2. The crack density is 0.1, aspect ratio is 0.035, and the friability changes from 0 to 0.99 with 0.2 increment.

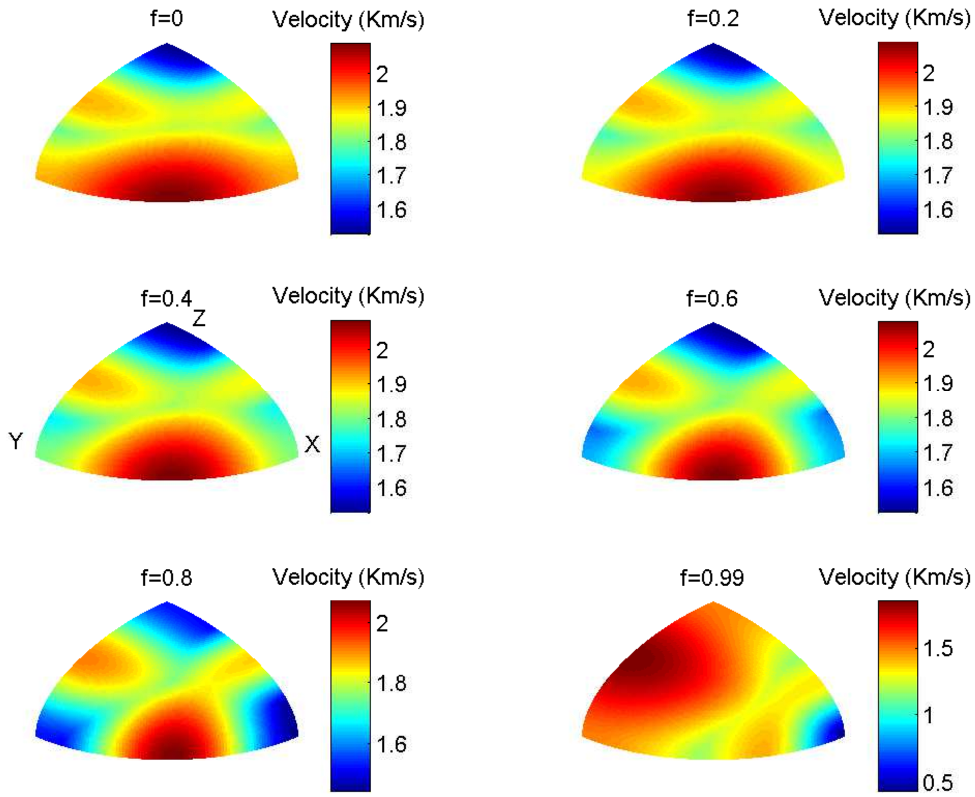

Figure 3.13: S_2 wave phase velocities variation with friability in water-saturated fractured orthorhombic medium.

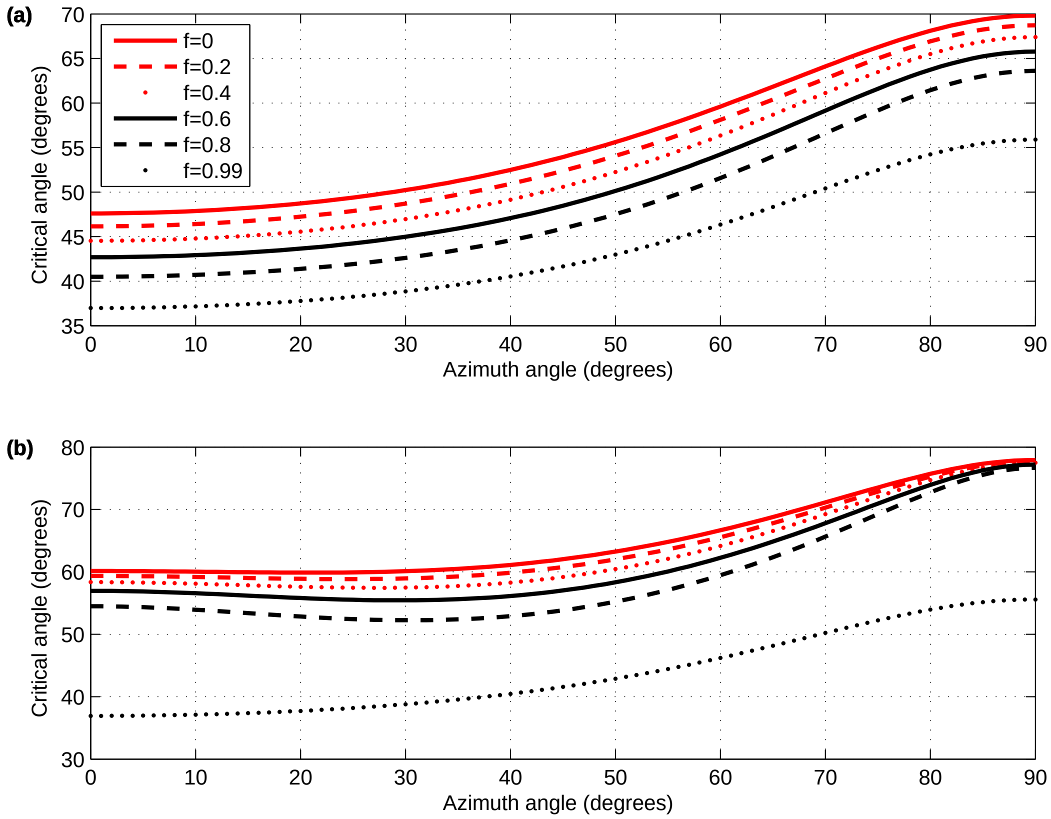

Figure 3.14: PP wave critical angle from the fractured fluid-saturated orthorhombic medium and background VTI medium: (a) gas-saturated upper layer; (b) water-saturated upper layer.

angle reflectometry gains more attention in extracting anisotropic parameters due to the available of high resolution seismic data. Landrø and Tsvankin (2007) show the P wave critical angle's sensitivity to Thomsen's parameters in VTI and orthorhombic media. Sil and Sen (2009) analyze the critical angle in the τ-p domain for anisotropic parameters estimation.

Figure 3.14 shows the friability variation with critical angles of PP reflection between gas and water-saturated orthorhombic and VTI media. Since P wave velocity generally decreases as friability increases, friability equals zero corresponds to the largest critical angle. Since zero azimuth angle corresponds to the lowest velocity and 90° azimuth angle corresponds to the highest velocity at the upper layer, the critical angles mostly increase with azimuth. Water-saturated medium has higher velocity than gas-saturated medium, thus it also has larger critical angle. Almost all critical angles increase monotonically with friability, exceptions are when friability equals 0.4, 0.6, and 0.8 in the water-saturated medium.

3.5.6 Friability variation with general anisotropic reflection coefficients

In this section, based on the previous method, I analyze the PP reflection coefficient between an orthorhombic fractured medium and an underlying VTI medium.

Validation of the computer code

Approximate perturbation reflection coefficient formula (Vavrycuk and Psencik, 1998) produces close results. When P wave incident on medium with upper and lower layers of VTI symmetry, it doesn't generate reflected SH wave. Also, the reflected P wave amplitude is azimuthally invariant. Tests in VTI/VTI medium generate almost zero SH wave reflection coefficient and no azimuthal reflection coefficient variation, the extra error is due to the modification of VTI symmetry to avoid shear wave singularities. If the medium is rotated azimuthally with certain angle according to Bond transformation, the calculated results should also rotate azimuthally with the same angle (Mavko et al., 2003). My computation results follow this rule. My numerical results also agree with the numerical results produced from the code written by Grechka (2002).

PP reflection coefficient between a gas-saturated orthorhombic medium and VTI medium

Figure 3.15 shows friability variation with exact PP reflection coefficient between a fractured gas-saturated orthorhombic medium and VTI medium with azimuth angle equals 0°, 30°, 60°, and 90°. A contour plot is shown in Figure 3.16. The maximum incidence angle equals 35°. Generally speaking, stiffness-tensor decreases as friability increases in the upper layer, so reflection coefficient increases. This four plots agree with this intuition. The separation of reflection coefficient at large incidence angle is not more obvious than at smaller incidence. Consequently, normal incidence reflection coefficient is enough to detect the friability variation in gas-saturated reflection problem. From Figure 3.16, we can see azimuthal variation of reflection coefficients are obvious at very small and large friability; at intermediate friability, the reflection coefficient is somewhat closer to azimuthally invariant for small incidence angle.

PP reflection coefficient between a water-saturated orthorhombic medium and VTI medium

Figure 3.15 shows friability variation with PP reflection coefficient between a fractured water-saturated orthorhombic medium and VTI medium. Azimuth and incidence angle are the same as the gas-saturated situation. Contour plots are shown in Figure 3.18. Crossover of reflection coefficient is observed for small azimuth angle (0° or 30°). This means at these two azimuthal angles, initially large friability corresponds to large reflection coefficient, but after around 10° incidence angle, small friability corresponds to large reflection coefficient. However, for large azimuth angle (60° or 90°), large friability almost always correspond to large reflection coefficient except around 20° incidence angle and 60° azimuth angle. Azimuthal variation of

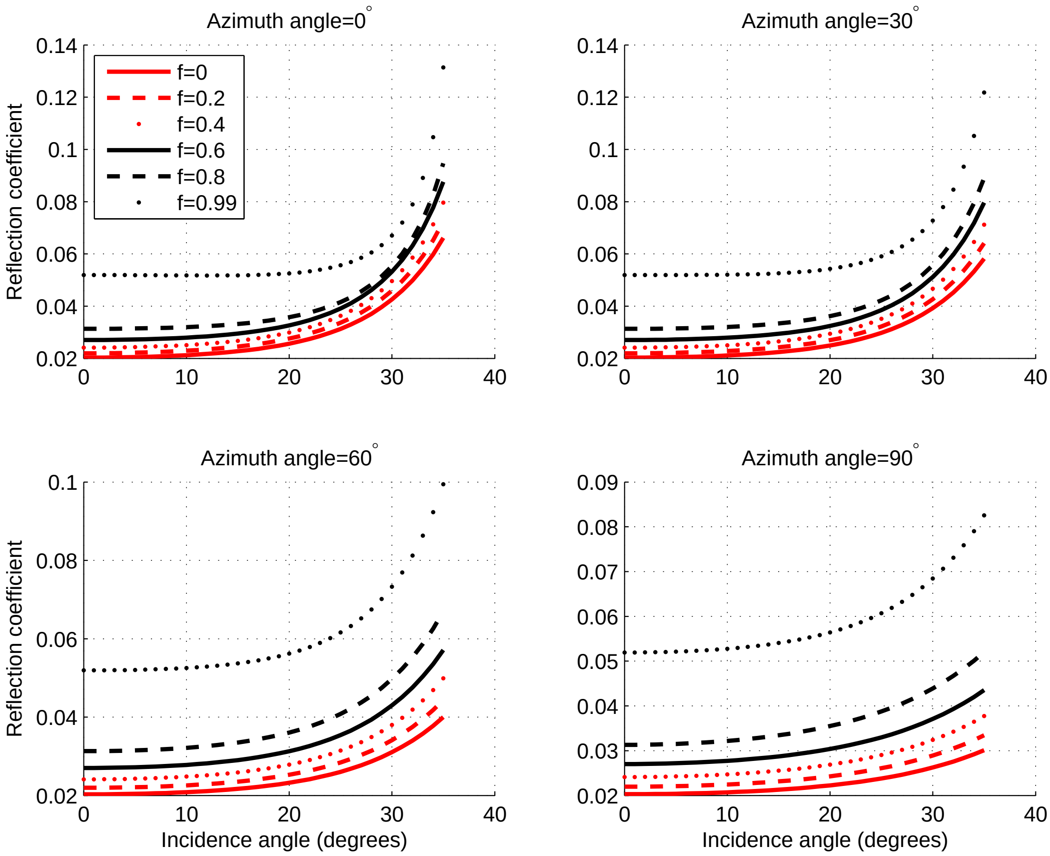

Figure 3.15: PP reflection coefficient between a fractured gas-saturated orthorhombic medium and VTI medium. The orthorhombic medium is the same as the medium analyzed in the previous section, the underlying VTI medium is the same as the background VTI medium to build the orthorhombic medium.

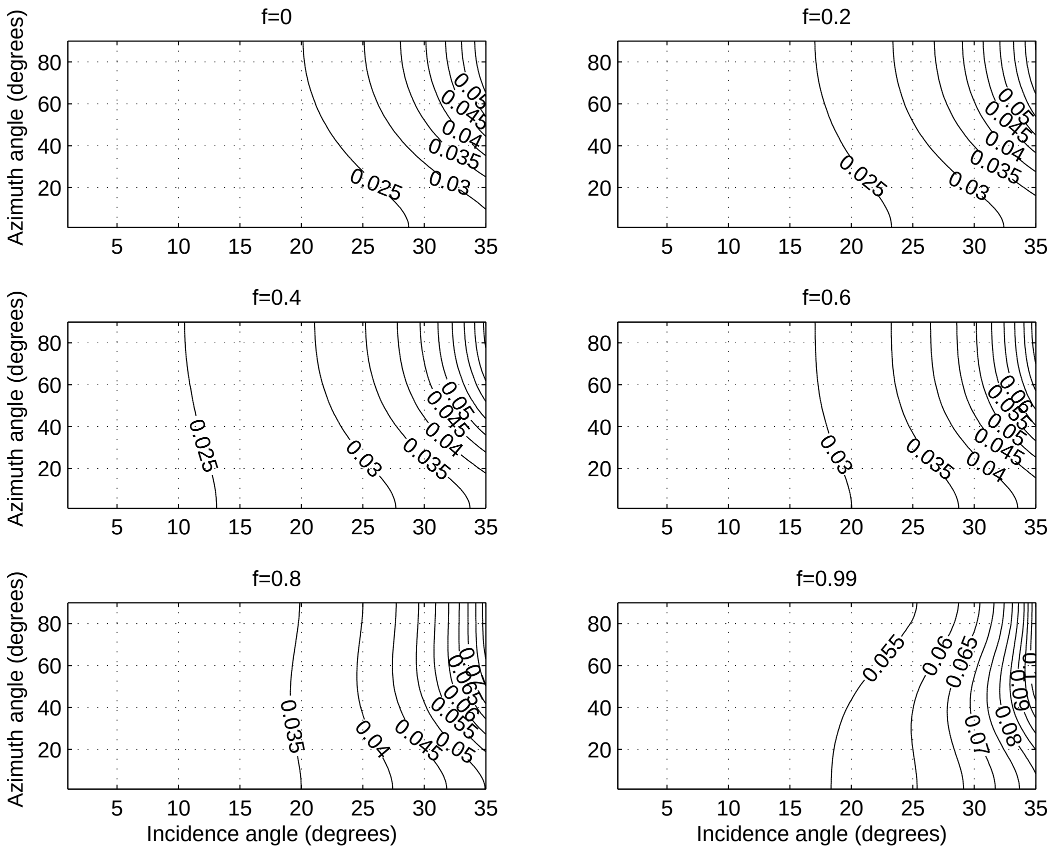

Figure 3.16: Contour plot of PP reflection coefficient between a fractured gas-saturated orthorhombic medium and VTI medium with different friability. The input parameters are the same as Figure 3.15.

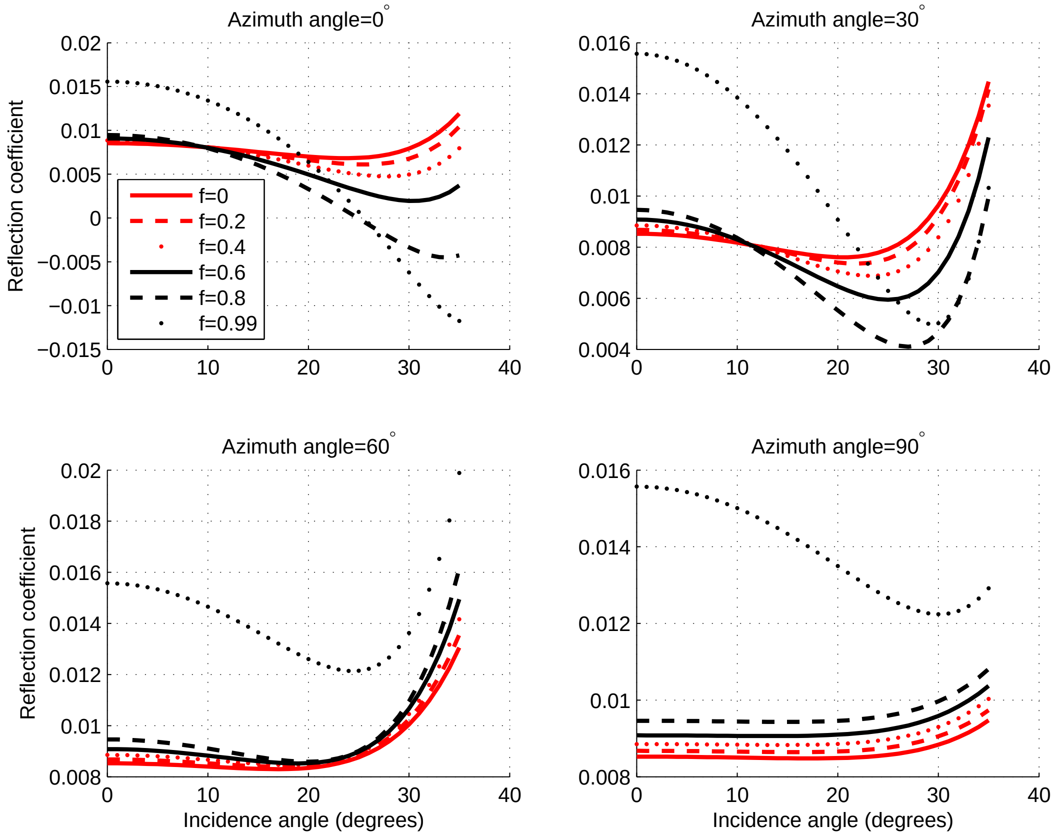

Figure 3.17: PP reflection coefficient between a fractured water-saturated orthorhombic medium and VTI medium. The orthorhombic medium is the same as the medium analyzed in the previous section, the underlying VTI medium is the same as the background VTI medium to build the orthorhombic medium.

PP reflection coefficient is very large for water-saturated medium of any friability.

A medium saturated with gas has obvious less moduli than saturated with water. Accordingly, the impedance contrast between the upper and lower layers is smaller for water-saturated medium. Smaller impedance contrast makes water-saturated medium generally has smaller reflection coefficient than gas-saturated medium. This character is observed on the four PP reflection coefficient figures. Overall, reflection coefficient characteristics in the water-saturated medium is very different from the gas-saturated medium with the same fracture and background medium parameters.

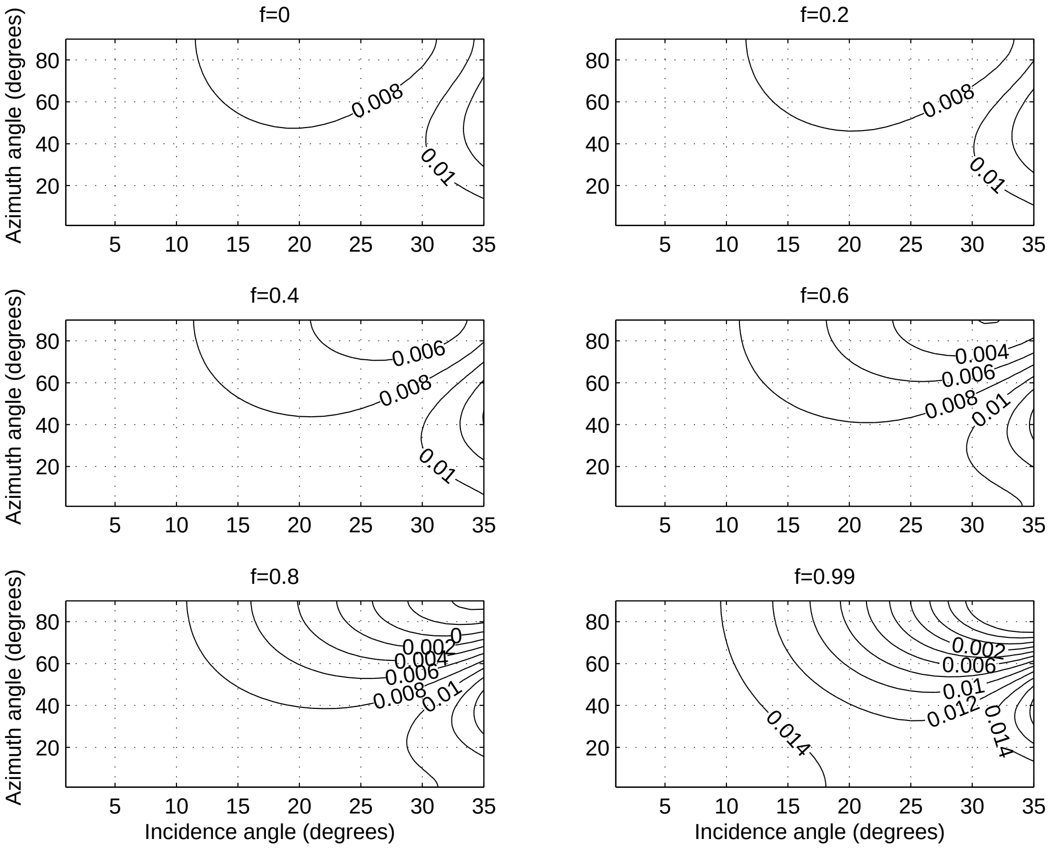

Figure 3.18: Contour plot of PP reflection coefficient between a fractured water-saturated orthorhombic medium and VTI medium with different friability. The input parameters are the same as Figure 3.17.

3.6 Conclusions

GSA modeling of porous medium's friability has observable seismic signatures, most of these signatures have very large, non-monotonic, and nonlinear variations:

1, as friability increases, most stiffness-tensor components decrease in both media;

2, most extended Thomsen's parameters decrease as friability increases. ϵ^2, γ^2, δ^2, and δ^3 in gas-saturated medium and ϵ^1, δ^2, and δ^3 in water-saturated medium are very sensitive to friability, while others are not;

3, P and S_1 waves have quasi vertical symmetry axis for both gas and water-saturated media with small friability, while large friability makes P and S_1 waves in both gas and water-saturated media have quasi horizontal symmetry axis. For the S_2 wave in both media, phase velocity surfaces show large variations and little transverse isotropy. There are sophisticated relationships between phase velocity and friability out of the symmetry plane, especially for S_2 wave;

4, zero friability corresponds to the largest critical angle and critical angles mostly increase as azimuth angle increases;

5, normal incidence reflection coefficient is enough to detect the friability variation in gas-saturated reflection problem. Additionally, azimuthal variation of reflection coefficient in gas-saturated medium also depends strongly on friability. Azimuthal variation of PP reflection coefficient is very large for water-saturated medium of any friability.

These conclusions are only limited to my specific situation, extension of these observations may not work if the medium parameters are not close to mine.

Chapter 4

Influence of Fame Inelasticity on Poroviscoelastic Reflections From a Gas-Water Contact

4.1 Introduction

Frequency-dependent phenomena are widely studied in seismology. Viscoelasticity, Biot's theory, and local flow are the three main groups for studying velocity dispersion and attenuation in fluid-saturated rocks (Müller et al., 2010). Viscoelastic theory is a phenomenological theory without consideration of microscopic, mesoscopic, or macroscopic rock structures. Further, Biot's theory (Biot, 1956a,b) predicts frequency-dependent velocity and attenuation of saturated rock from dry rock and fluid properties. They are two classical but entirely different approaches for investigating frequency-dependent seismic signatures. However, they can be combined to produce the poroviscoelastic (hereafter refer as PVE) model.

Plane wave reflection and transmission (hereafter refer as R/T) problem can be studied in both viscoelastic and Biot media: plane wave R/T in viscoelastic media was studied by Ursin and Stovas (2002), Krebes and Daley (2007), and many others, while Biot reflection was studied by Deresiewicz (1960), Dutta and Ode (1983), Liner (2012), and many others. The frame inelasticity is considered to be important in both laboratory (Bouzidi and Schmitt, 2012) and field work (Stoll and Kan, 1981) for calculating PVE reflection coefficient. However, these works consider the interface between a water and PVE medium, which are mostly suitable for oceanic floor applications. A theory is lacking in analyzing the influence of frame inelasticity on the plane wave reflection between two PVE media. Since most earth layers are not water but porous media, this approach is more general. It also corresponds directly to the classical Zoeppritz equations in elastic medium.

First I briefly review the theory that constitutes PVE model, then I introduce the method of PVE reflection calculation, finally I give some numerical results and discussions about the influence of frame inelasticity on PVE dispersions, attenuations, reflections, and transmissions.

4.2 Poroviscoelastic dispersion and attenuation

4.2.1 Biot dispersion and attenuation

Because PVE model is a synthesis of Biot theory and viscoelasticity, here I give a brief review of the Biot theory. Biot theory is based on the Lagrangian formulation of kinetic and dissipation energy function (Biot, 1956a,b, 1962). The equations of motion are:

$$\begin{aligned}
&(\lambda + \alpha^2 M + \mu)\nabla(\nabla \bullet \mathbf{u}) + \mu\nabla^2\mathbf{u} + \alpha M\nabla(\nabla \bullet \mathbf{W}) = \frac{\partial^2}{\partial t^2}\left(\rho\mathbf{u} + \rho_f\mathbf{W}\right) \\
&\alpha M\nabla(\nabla \bullet \mathbf{u}) + M\nabla(\nabla \bullet \mathbf{W}) = \frac{\partial^2}{\partial t^2}\left(\rho_f\mathbf{u} + \frac{S\rho_f}{\beta}\mathbf{W}\right) + b\frac{\partial \mathbf{W}}{\partial t}
\end{aligned} \tag{4.1}$$

here $\mathbf{u}$ is the matrix displacement, $\mathbf{W}$ is the relative displacement between matrix and fluid multiplied by porosity, and α is the Biot-Willis' coefficient. α and M are

Symbol	Physical meaning	Value
K_s	bulk modulus of the matrix	3.5×10^{10}
K_{fr}	bulk modulus of the frame	1.7×10^{9}
μ	shear modulus of the frame	1.855×10^{9}
K_f	bulk modulus of gas/water	$2.2\times10^{7}/2.4\times10^{9}$
ρ	bulk density with gas/water saturation	1885/2155
ρ_f	density of gas/water	100/1000
η	viscosity of gas/water	$1.5\times10^{-5}/0.001$
β	porosity	0.3
κ	permeability	9.86923×10^{-13}
a	pore size	8.1114×10^{-6}
S	tortuosity	2.1667

Table 4.1: The parameters for Biot medium, gas, and water. The units are International System of Units.

expressed by equation 4.2. The meanings of some other parameters are in Table 4.1.

$$\begin{aligned} \alpha &= 1 - \frac{K_{fr}}{K_s} \\ M &= \frac{K_s^2}{K_s[1+\beta(\frac{K_s}{K_f}-1)] - K_{fr}} \end{aligned} \tag{4.2}$$

By solving Euler's equation in a three dimensional tube, I get $b = \frac{\eta}{\kappa}F(\zeta)$, $F(\zeta) = \frac{1}{4}(\frac{\zeta T(\zeta)}{1+2iT(\zeta)/\zeta})$, $T(\zeta) = \frac{\mathrm{e}^{i3\pi/4}\mathrm{J}_1(\zeta \mathrm{e}^{-i\pi/4})}{\mathrm{J}_0(\zeta \mathrm{e}^{-i\pi/4})}$, and $\zeta = (\omega/\omega_r)^{1/2} = (\frac{\omega a^2 \rho_{fl}}{\eta})^{1/2}$. J_0 and J_1 are the zero and first order Bessel functions of the first kind. F is the frequency correction factor, which equals one for zero frequency. I incorporate the frequency correction factor since it may have considerable influence on R/T coefficients in the acoustic logging frequency range (Santos et al., 1992). Additional two parameters tortuosity S (Berryman, 1980) and pore size parameter a (Hovem and Ingram, 1979) are determined as:

$$S = 1 - 0.5 \times (1 - 1/\phi)$$

$$a = 2\sqrt{5\kappa/\phi}$$

Essentially, the calculation of Biot dispersion and attenuation is a process of solving differential equations 4.1. The medium is isotropic, so I can use Helmholtz decomposition to get the displacement potential functions. Next with the assumption of periodic plane waves, and after some manipulation of equation of motion and Helmholtz decomposed displacements, I have (Carcione, 2007; Mavko et al., 2003):

$$\frac{1}{V^2} = \frac{-(HL+M\rho-2\alpha M\rho_f)\pm\sqrt{(HL+M\rho-2\alpha M\rho_f)^2-4(\alpha^2M^2-MH)(\rho_f^2-\rho L)}}{2(\alpha^2M^2-MH)} \tag{4.3}$$

in which $H = \lambda + \alpha^2 M + 2\mu$ and $L = \dfrac{S\rho_f}{\beta} + \dfrac{bi}{\omega}$. These two velocities correspond to the fast and slow P waves. $L = \dfrac{S\rho_f}{\beta} - \dfrac{bi}{\omega}$ in Carcione (2007) and Mavko et al. (2003), this is because of different assumption of the plane wave phases. Physically, this means dispersion in Biot theory is dependent on the plane wave phase. The S wave velocity is:

$$\frac{1}{V^2} = \frac{\rho L-\rho_f^2}{\mu L}$$

The attenuation properties of rocks are measured through the inverse quality factor:

$$\frac{1}{Q} = \frac{M_I}{M_R}$$

4.2.2 Frame inelasticity

The synthesis of viscoelasticity and Biot theory is through modifying some poroelastic parameters into complex numbers. After the synthesis, the PVE model still relates the dry to saturated moduli, similar to Biot's theory and Gassmann's equation. Rasolofosaon (1991) modifies the parameter H, which corresponds to the modulus of no relative motion between solid and fluid. H is also the effective saturated compressional wave modulus in Gassmann's equation. Carcione (1998) and Carcione and Helle (1999) modify the modulus M that couples solid and fluid modulus into complex number. However, their M and H values are based on assumption. As a deduction, their results may be far from realistic. For example, Rasolofosaon (1991) uses a standard linear solid model to simulate the dry moduli, but the parameters quality factor and relaxation frequency are subjective.

In other respects, lots of experimental data show little dry rock quality factor variation with frequency (Born, 1941; Toksöz et al., 1979; Spencer Jr, 1981; Tisato and Quintal, 2013). And Bourbie et al. (1987) claim the dry rock attenuation should not be excluded for experimental data interpretation. Therefore, I take the simple method of direct modifications of dry moduli K_{fr} and μ_{fr} into complex ones. The modification also leads to the changing of λ, α, H, and M from real into complex moduli. Since the characteristics of fluid doesn't change, the study of frame inelasticity should be helpful for better characterization of fluid properties.

4.3 Poroviscoelastic reflection and transmission coefficients

The PVE R/T problem is similar to poroelastic R/T problem, while the poroelastic R/T coefficients calculation is similar to the Zoeppritz equation, they are both from the matching of boundary conditions. Using poroelastic R/T coefficients to study rock properties dates back to Deresiewicz (1960). These studies are based on Biot theory or some approximations (Geertsma and Smit, 1961; Denneman et al., 2002; Silin and Goloshubin, 2010) to suit for specific rocks. Among the rock properties, viscous coupling (Yang and Sato, 1998), fluid flow condition (Wu et al., 1990; Yang,

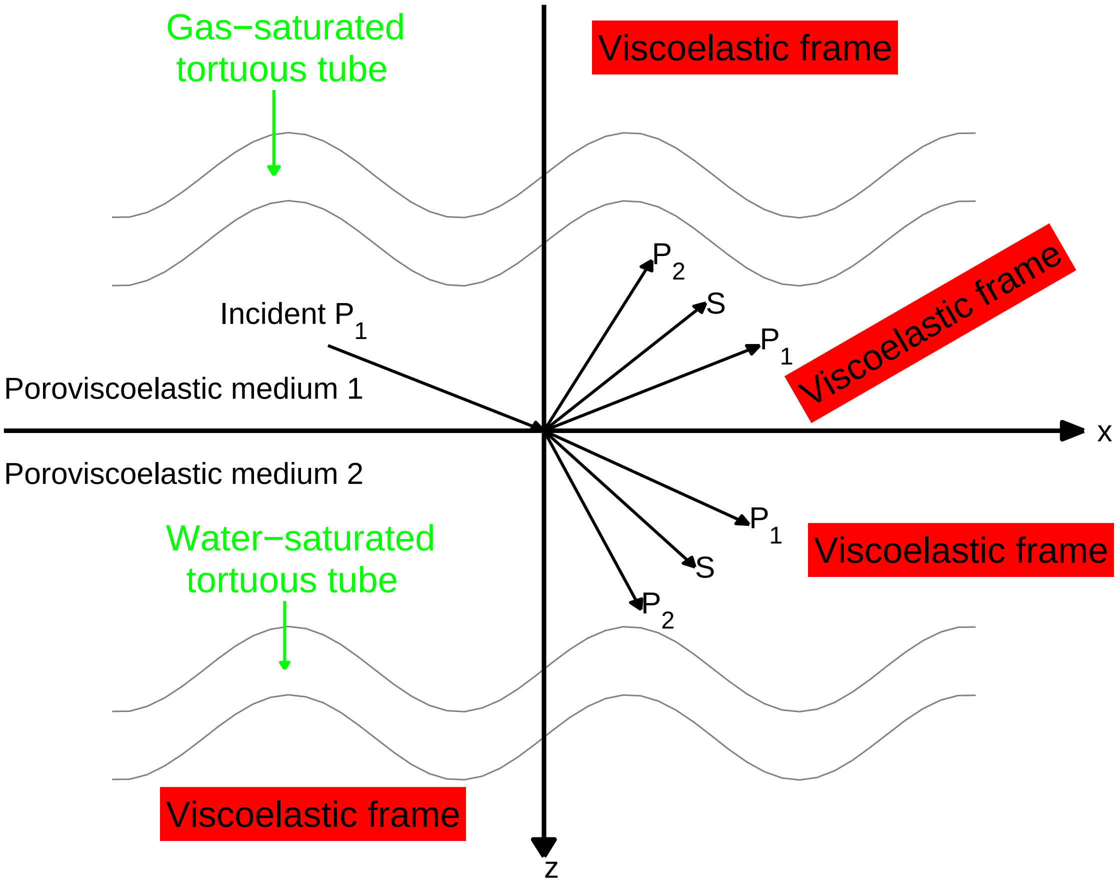

Figure 4.1: P wave reflection between two PVE media has three reflected and transmitted waves, including slow P waves.

1999; Denneman et al., 2002), fluid saturation (Yang and Sato, 2000; Quintal et al., 2011), pore pressure (Carcione, 2007), and frequency correction factor F (Santos et al., 1992) were studied. Dutta and Ode (1983) pay particular attention to slow P wave.

Similar to the poroelastic R/T problem, I study a plane fast compressional wave incident on a horizontal interface, which generates six reflected and transmitted waves including the slow P waves. It is schematically shown in Figure 4.1. Then six boundary conditions are established for solving for the six waves' amplitude. The

boundary conditions follow from the balance of power input per unit area across the interface (Deresiewicz and Skalak, 1963; Dutta and Ode, 1983; Carcione, 2007). The modification of Biot theory into PVE theory doesn't change these conditions:
1, continuity of matrix horizontal velocity;
2, continuity of matrix normal velocity;
3, continuity of relative normal velocity between frame and fluid multiplied by porosity;
4, continuity of fluid pressure;
5, continuity of shear total stress;
6, continuity of normal total stress.

Zoeppritz equations' boundary conditions use continuity of displacements instead of velocities, which are same as the velocities boundary conditions 1 and 2 used here. This is due to the common frequency denominator. I am using an open boundary condition here, which is strongly related to high permeability and connected pores. If relative normal velocity between frame and fluid is zero, then it is a closed boundary condition, which makes the slow compressional wave hard to observe experimentally (Rasolofosaon, 1988).

After some manipulations of boundary conditions, I have the equations that can be solved for the six R/T coefficients:

$$\begin{pmatrix} \sin\alpha & \sin\beta & \cos\gamma & -\sin\alpha' & -\sin\beta' & \cos\gamma' \\ -\cos\alpha & -\cos\beta & \sin\gamma & -\cos\alpha' & -\cos\beta' & -\sin\gamma' \\ \tau_{11}\cos\alpha & \tau_{12}\cos\beta & -\tau_{13}\sin\gamma & \tau_{21}\cos\alpha' & \tau_{22}\cos\beta' & \tau_{23}\sin\gamma' \\ \frac{M_1(\alpha_1+\tau_{11})}{V_{11}} & \frac{M_1(\alpha_1+\tau_{12})}{V_{12}} & 0 & -\frac{M_2(\alpha_2+\tau_{21})}{V_{21}} & -\frac{M_2(\alpha_2+\tau_{22})}{V_{22}} & 0 \\ \frac{\mu_1\sin 2\alpha}{V_{11}} & \frac{\mu_1\sin 2\beta}{V_{12}} & \frac{\mu_1\cos 2\gamma}{V_{13}} & \frac{\mu_2\sin 2\alpha'}{V_{21}} & \frac{\mu_2\sin 2\beta'}{V_{22}} & -\frac{\mu_2\cos 2\gamma'}{V_{23}} \\ X_1 & X_2 & X_3 & X_4 & X_5 & X_6 \end{pmatrix} = M \tag{4.4}$$

$$M \times \begin{pmatrix} A_1 \\ A_2 \\ A_3 \\ A_4 \\ A_5 \\ A_6 \end{pmatrix} = \begin{pmatrix} -\sin\alpha \\ -\cos\alpha \\ \tau_{11}\cos\alpha \\ -\frac{M_1(\alpha_1+\tau_{11})}{V_{11}} \\ \frac{\mu_1\sin 2\alpha}{V_{11}} \\ X_7 \end{pmatrix} \tag{4.5}$$

in which:

$$
\begin{cases}
X_1 = \frac{\lambda_1+\alpha_1^2 M_1+\alpha_1 M_1\tau_{11}}{V_{11}} + 2V_{11}\mu_1(p_3^r)^2 \\
X_2 = \frac{\lambda_1+\alpha_1^2 M_1+\alpha_1 M_1\tau_{12}}{V_{12}} + 2V_{12}\mu_1(p_3^{r2})^2 \\
X_3 = -2V_{13}\mu_1 p_1^{rs} p_3^{rs} \\
X_4 = -\frac{\lambda_2+\alpha_2^2 M_2+\alpha_2 M_2\tau_{21}}{V_{21}} - 2V_{21}\mu_2(p_3^t)^2 \\
X_5 = -\frac{\lambda_2+\alpha_2^2 M_2+\alpha_2 M_2\tau_{22}}{V_{22}} - 2V_{22}\mu_2(p_3^{t2})^2 \\
X_6 = -2V_{23}\mu_2 p_1^{ts} p_3^{ts} \\
X_7 = -\frac{\lambda_1+\alpha_1^2 M_1+\alpha_1 M_1\tau_{11}}{V_{11}} - 2V_{11}\mu_1(p_3)^2
\end{cases}
$$

In these equations, A corresponds to R/T coefficients. α, β, γ, α', β', and γ' mean the angles of reflected P_1, reflected P_2, reflected S, transmitted P_1, transmitted P_2, and transmitted S waves, respectively. τ is the amplitude ratio of potential functions of relative displacement between fluid and solid multiplied by porosity over solid displacement. V_{11}, V_{12}, and V_{13} are velocities of P_1, P_2, and S waves in the upper medium; V_{21}, V_{22}, and V_{23} are velocities of P_1, P_2, and S waves in the lower medium. p means horizontal slowness. Notice α is both the Biot-Willis coefficient and incidence angle. Other parameters' meanings are in Table 4.1. Solving this equation, I can get the R/T coefficients for PVE media, and energy coefficients of each wave mode can be calculated subsequently. However, since displacement instead of energy is the most frequently considered factor in current seismic amplitude interpretation (Hilterman, 2001), I will only consider displacement. The computation of transmission coefficient is useful for computing reflection coefficients of multilayered medium. At the same time, it is also helpful for characterizing laboratory ultrasonic experiment if transmitted data is measured (Plona, 1985).

4.4 Numerical results

Numerical results of the influence of frame inelasticity on PVE dispersion, attenuation, and reflection with gas or water saturation are presented here. The Biot model parameters except pore size and tortuosity are from the widely used Dutta and Ode data (Dutta and Ode, 1979), which is listed in Table 4.1. Due to the lack of dry moduli attenuation data, I study the influence of frame inelasticity with Q_{fr} equals 10, 20, 40, and 80, respectively, which tries to mimic most range of Q_{fr} in sandstone (Toksöz et al., 1979; Tao et al., 1995). The variation makes the examination of the frame inelasticity's influence on R/T coefficients more convenient. In the meanwhile, the quality factor range also tries to at least include the realistic situation. The PVE attenuation is the addition of the attenuation caused by the viscoelastic and poroelastic mechanisms.

4.4.1 Poroviscoelastic dispersions and attenuations

Numerical results of dispersions and attenuations are plotted in Figure 4.2 with gas saturation and Figure 4.3 with water saturation.

P and S wave dispersions are similarly and less influenced by frame inelasticity variations than attenuations. In Biot attenuation, very low frequency (1-1000 Hz) has extremely small attenuation, which is contradictory to some experimental results (Dvorkin and Nur, 1993). The PVE model corrects this contradiction that can provide a possible better agreement with experimental results. For gas-saturated sand, Biot attenuation is ignorable even with small frame inelasticity; for water saturation, Biot attenuation is still small compared with overall attenuation. Compared to Rasolofosaon (1991), different viscoelastic frame model such as stand linear solid model and poroelastic parameter such as H doesn't influence the characteristics that

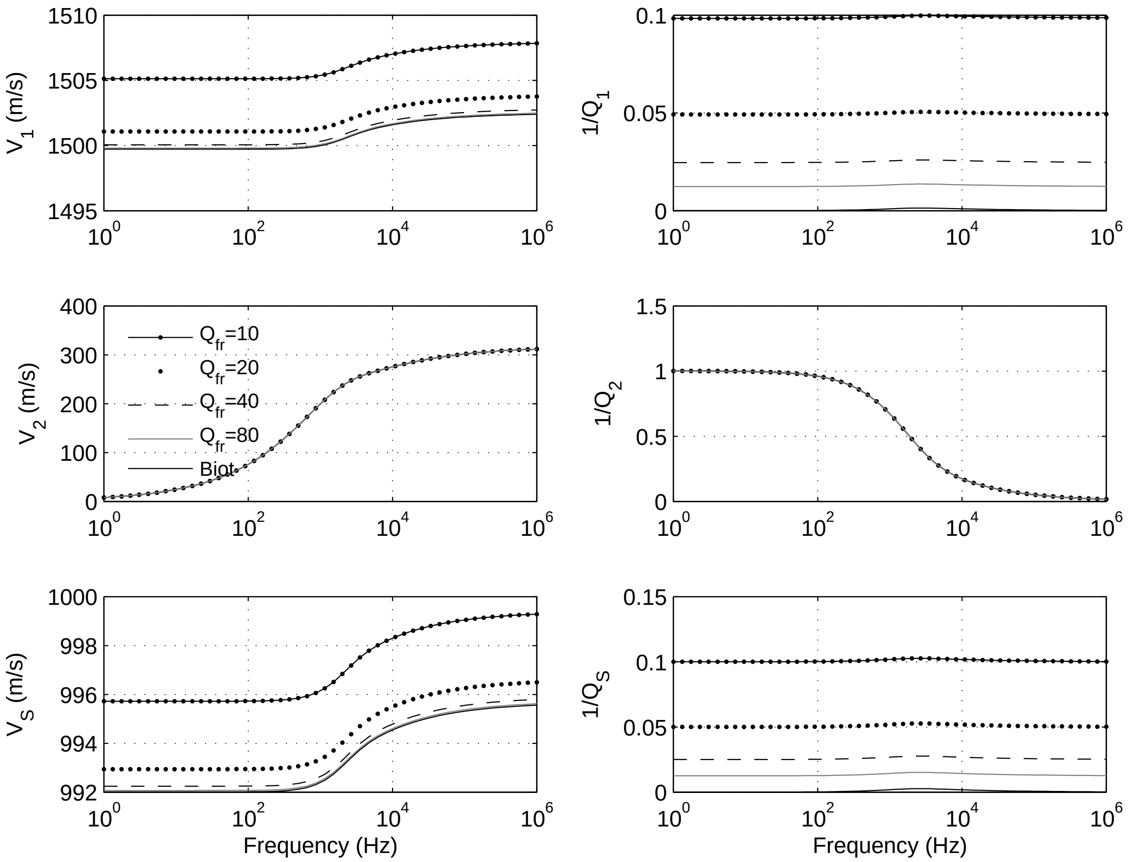

Figure 4.2: Biot and poroviscoelastic dispersions and attenuations for P_1, P_2, and S waves with gas saturation. Dry rock and saturating fluid parameters are in Table 4.1.

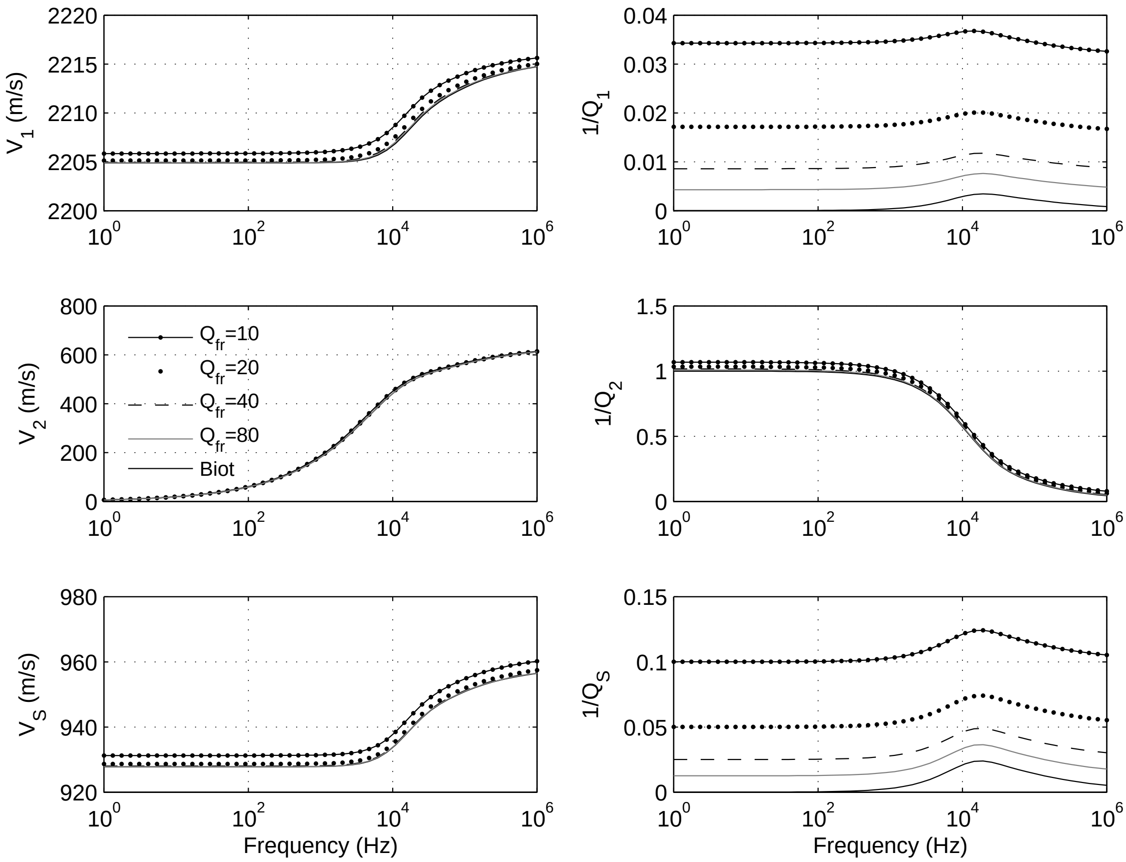

Figure 4.3: Biot and poroviscoelastic dispersions and attenuations for P_1, P_2, and S waves with water saturation. Dry rock and saturating fluid parameters are in Table 4.1.

overall PVE attenuation basically equals the addition caused by frame inelasticity and poroelasticity. They are not perfectly equal to each other due to the definition of attenuation.

Biot slow wave is a diffusive wave and mostly related to the fluid, thus in both gas and water saturation, slow wave velocities and inverse quality factors are almost not influenced by frame inelasticity variations. An exception is the attenuation of water-saturated rock with strong frame inelasticity (Q=10), which have a small relative deviation from Biot attenuation of about 7% in the low and intermediate frequency band; the slow wave relative attenuation deviation at the high frequency range is large, which is due to low level of Biot attenuation.

4.4.2 Poroviscoelastic reflection and transmission coefficients

Following Dutta and Ode (1983), I choose the typical seismic frequency 100 Hz and high frequency 10^5 Hz and compare between Biot and PVE R/T coefficients. The upper layer is gas-saturated and the lower layer is water-saturated. R/T coefficients over the same frequency range and different incidence angles are plotted in Figure 4.4 and 4.5. R/T coefficients over the same incidence angle and different frequencies are plotted in Figure 4.6 and 4.7. R/T coefficients in these two plots change smoothly at low frequency and abruptly from the neighborhood of 10^4 Hz, which is also the frequency range of the largest velocity variations and attenuations.

Figure 4.4 shows normal incidence R/T coefficients over 1-10^6 Hz. As the frame inelasticity increases, almost all R/T coefficients decrease; exceptions are P_1 reflection coefficient has irregular variations at very high frequency and P_2 reflection coefficient increases if the frequency is less than around 10^3 Hz. P_1 wave reflection coefficient has maximal decreasing of 6.5% around 10^4 Hz, which means this coefficient also has the largest absolute coefficient decreasing. Although the absolute fluctuation of P_2 reflection coefficient is small over all frequency range, the maximal

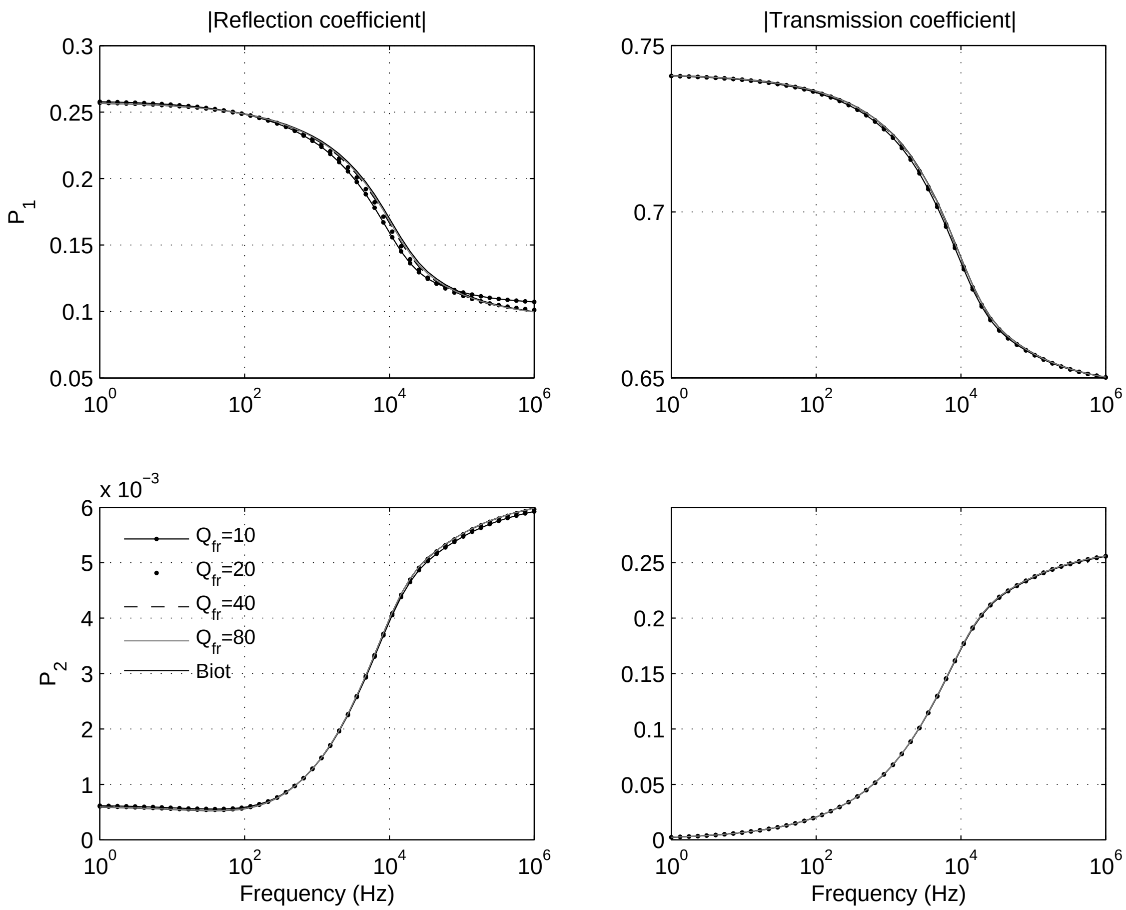

Figure 4.4: Poroviscoelastic normal reflection and transmission coefficients from a gas-water contact with different dry rock quality factor and frequencies. S wave with zero reflection and transmission coefficients are not shown.

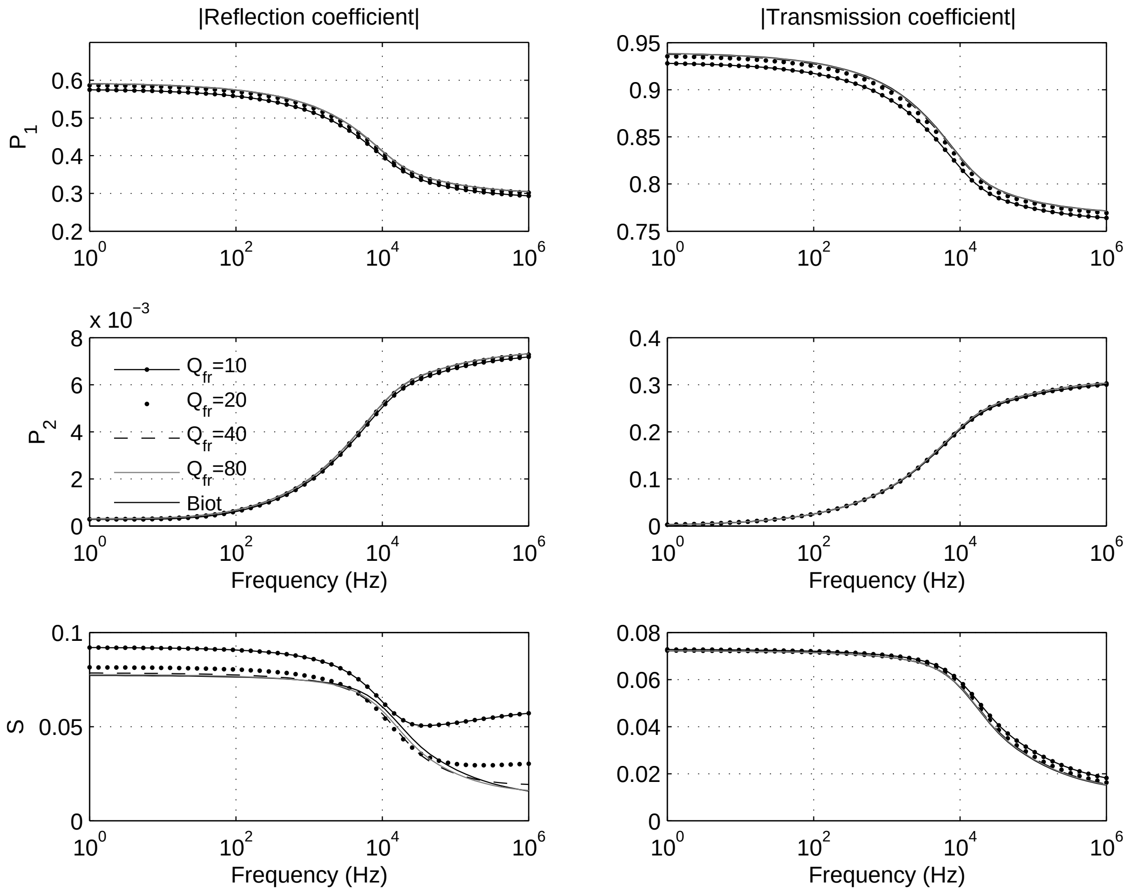

Figure 4.5: 40° incidence poroviscoelastic reflection and transmission coefficients from a gas-water contact with different dry rock quality factor and frequencies.

relative reflection coefficient increases about 6% between 10-100 Hz. Very small maximal absolute and relative decreasing is observed of transmission coefficient.

The R/T coefficients of P_1 wave with $40°$ incidence are plotted in Figure 4.5. P_1 wave incidence critical angle is about $43°$, so these results are still less than the critical angle. The results have obvious larger overall absolute deviation from Biot reflection than normal incidence, which can also be seen on Figure 4.6 and 4.7. P_1 reflection coefficient has the largest absolute difference from Biot reflection than other R/T coefficients of the low frequency range (1-10^3 Hz). Counting clockwise from P_1 wave reflection coefficient, largest relative fluctuations are on the order of decreases 4%, decreases 1.5%, decreases 17%, increases 2.6 times, increases 20%, and decreases 2% in the neighborhood of 10^6, 10^4, 10^4, 10^6, 10^6, and 10 Hz, respectively.

Figure 4.6 exhibits 100 Hz R/T coefficients over all incidence angle. P_1 and P_2 waves R/T coefficients have largest absolute deviations from the Biot reflection in the neighborhood of critical angle, while S wave R/T coefficients have largest absolute deviations from the Biot reflection around $65°$. Counting clockwise from P_1 wave reflection, maximal relative coefficient variations are on the order of decrease 20%, decrease 10%, decrease 10%, and decrease 10%, decrease 90%, and decrease 11%, respectively. Note S wave's R/T coefficients are zero at normal and grazing incidence due to the polarization of incidence P_1 wave. This observation is also applicable to Figure 4.7. The S wave reflection coefficient is particularly striking and noteworthy: it has the largest fluctuation from Biot reflection at 100 Hz of small incidence angle. Most current field seismic explorations satisfy the frequency and offset condition. Exploration seismologists should pay special attention to this feature if they wish to estimate the Biot theory parameters from converted S wave reflection coefficient.

10^5 Hz R/T coefficients over the entire incidence angle are in Figure 4.7. The results show similar characteristics to Figure 4.6 in terms of largest deviations from

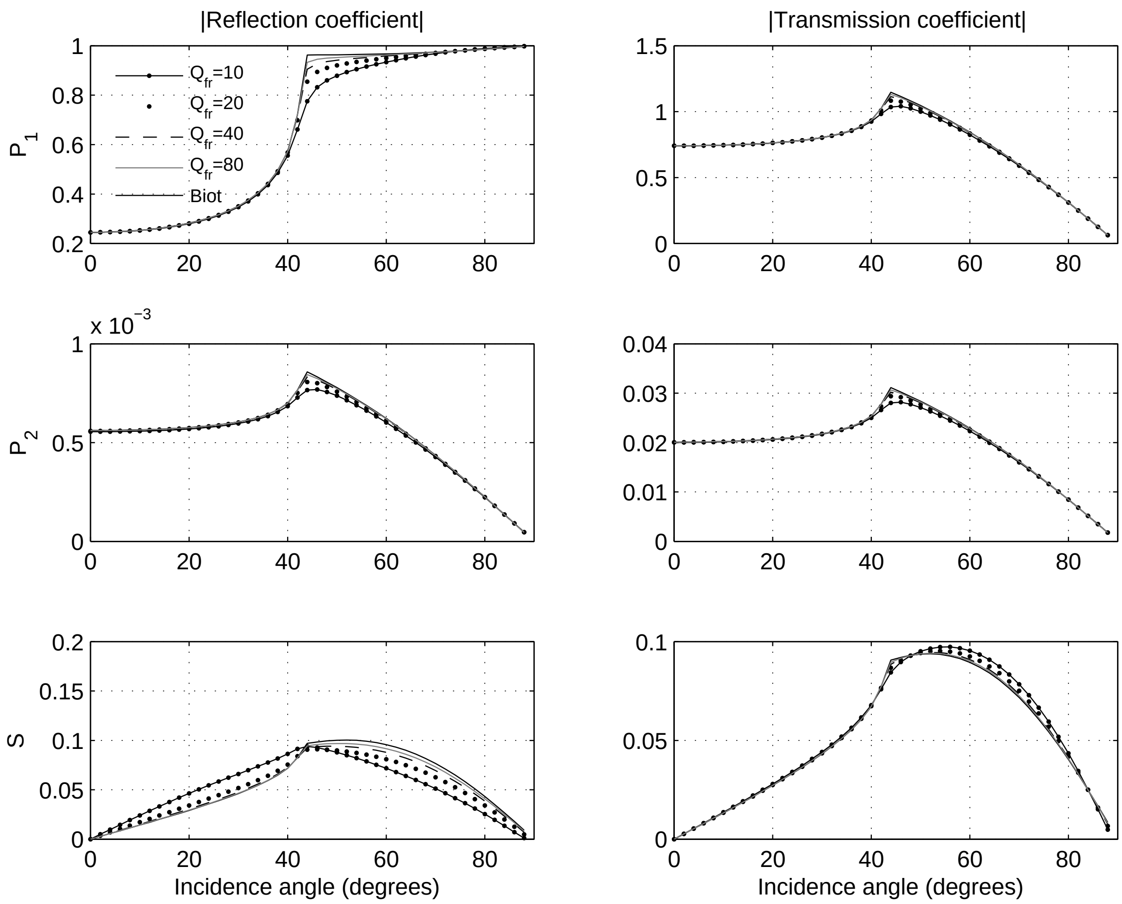

Figure 4.6: Poroviscoelastic reflection and transmission coefficients from a gas-water contact with different dry rock quality factor and incidence angles in 100 Hz.

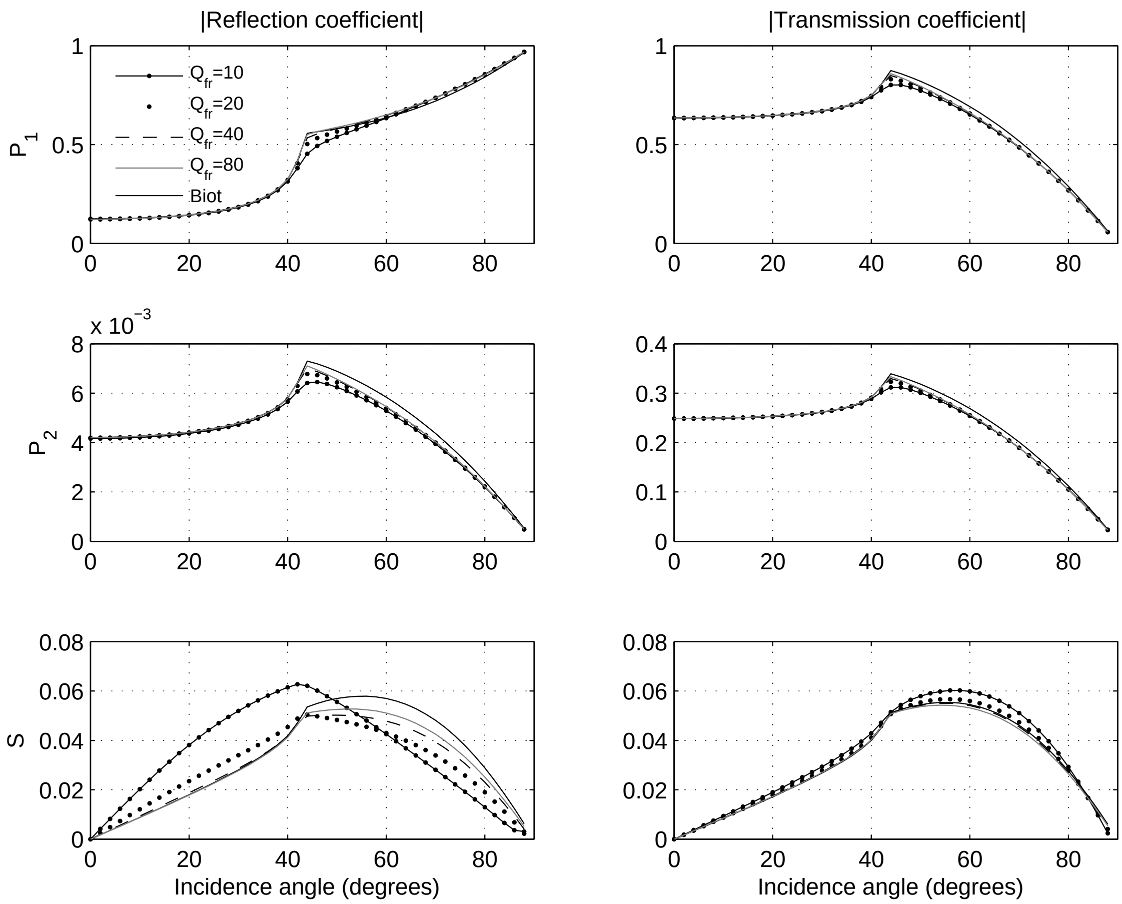

Figure 4.7: Poroviscoelastic reflection and transmission coefficients from a gas-water contact with different dry rock quality factor and incidence angles in 10^5 Hz.

Biot reflection except the S wave reflection coefficient also has large deviations at small incidence angle around 30°. Clockwise from P_1 wave reflection, maximal relative differences from Biot reflection are on the order of decrease 20%, decrease 8%, decrease 8%, decrease 6%, increase 1.2 times, and decrease 12%, respectively.

4.5 Discussion

The limitations of my research are: 1, plane wave approach may be not sufficient if the source and receiver are close, in this case, point source radiation pattern can be a good substitution (Tsvankin and Chesnokov, 1990); 2, geological structural may not be flat, thus an effective reflection coefficient may offer a more flexible modeling tool (Ayzenberg et al., 2007); 3, other factors such as anisotropy, nonlinearity, and hysteresis can be incorporated based on specific rock properties; 4, from the perspective of experimental data, for most dry rocks, $Q_P < Q_S$ (Toksöz et al., 1979), thus the assumption that the frame quality factor $Q_P = Q_S$ may need to be modified or measured directly; 5, influence of inhomogeneity angle (Carcione, 2007) is another factor that can be considered; 6, the pore size parameter and tortuosity can be measured instead of estimated (Bouzidi and Schmitt, 2012).

In places of large magnitude variations, such as near the critical angle, the modeling results are dependent on the sampling rate. Hence the results are a rough estimation.

4.6 Conclusions

This work studies poroviscoelastic AVO between a gas-water contact through analyzing the influence of frame inelasticity on Biot dispersion, attenuation, and reflection of a sand. Frame inelasticity has small influence on Biot P and S wave dispersion, and almost no influence on slow wave dispersion. Frame inelasticity has a substantial impact on the Biot P and S wave attenuation, and relatively small impact on Biot slow wave attenuation. At small and large incidence angles, frame inelasticity has small influence on Biot reflection; near critical angle, frame inelasticity has substantial impact on Biot reflection.

Some general remarks can be made about influence of frame inelasticity on PVE R/T coefficients. Firstly, stronger frame inelasticity generally causes larger differences from Biot reflection, and the maximal differences are all caused by largest frame inelasticity. Additionally, R/T coefficients are obviously deviated from Biot reflection only with strong dry modulus attenuation (Q_{fr}=10). Secondly, P_2 wave reflection coefficient is least influenced by frame inelasticity compare to P_1 and S R/T coefficients. Thirdly, similar to the purely elastic case (Krebes and Daley, 2007), introduction of frame inelasticity smooth out the Biot R/T coefficient's gradient discontinuities at critical angle. Lastly, normal incidence R/T coefficients fluctuation on average are smallest compare to other three cases.

In current geological situation and theoretical framework, the computed results show frame inelasticity is not ignorable for some geophysical applications. PP critical angle reflectometry and PS wave reflection coefficient at near offset are the best candidate tools for distinction of frame inelasticity. However, for normal incidence PP wave characterization, frame inelasticity is not that important.

Chapter 5

Conclusions and future work

My approach is proposed to distinguish between connected and disconnected pores through analysis of seismic signatures, especially AVO. Although the comparisons are not fully finished, this preliminary work may be considered as a starting point. The main results are:

Firstly, simple isotropic, homogeneous, and lossless medium is analyzed with regard to eight medium parameters. Results show the parameters all have significantly different sensitivity to reflection coefficient.

Secondly, I use General Singular Approximation to model friability's seismic signatures. The friability has observable seismic signatures, most of these signatures have very large, non-monotonic, and nonlinear variations. For my chosen model, I observe: 1, as friability increases, most stiffness-tensor components decrease in both media; 2, most extended Thomsen's parameters decrease as friability increases. ϵ^2, γ^2, δ^2, and δ^3 in gas-saturated medium and ϵ^1, δ^2, and δ^3 in water-saturated medium are very sensitive to friability, while others are not; 3, P and S_1 waves have quasi vertical symmetry axis for both gas and water-saturated media with small friability. Large friability makes P and S_1 waves in both gas and water-saturated media have quasi horizontal symmetry axis. For the S_2 wave in both media, phase velocity surfaces show large variations and little transverse isotropy.

The modeled results show sophisticated relationship between phase velocity and friability out of the symmetry plane, especially for S_2 wave; 4, friability equals zero corresponds to the largest critical angle and critical angles mostly increase as azimuth angle increases; 5, normal incidence reflection coefficient is enough to detect the friability variation in gas-saturated reflection problem, azimuthal variation of reflection coefficient in gas-saturated medium also depends strongly on friability. Azimuthal variation of PP reflection coefficient is very large for water-saturated medium of any friability.

Lastly, influence of frame inelasticity on wave dispersions, attenuations, and reflection and transmission coefficients are computed and analyzed in detail. The computed results use the data of a typical sand in the Gulf of Mexico with possible values of frame inelasticity. Plotted numerical results show frame inelasticity has considerable influence on reflection and transmission coefficients in some frequency and incidence angle range.

There are still additional space of working based on the following considerations:

1, there are many existing other theories that deals with pore connectivity. For example, Darcy's law deals with permeability, double porosity theory explicitly splits the porosity into connected and disconnected pores, and Biot-Willis parameter is related to rock consolidation (Jiang, 2013). Consequently, comparisons with these theories may reveal more insights about the friability parameter;

2, the anisotropic modeling algorithm is still preliminary and other signatures such as anisotropic Poisson's ratio, V_P/V_S, AVO gradient, moveout velocity, converted mode wave, shear wave, spherical wave, surface wave, interface curvature, pore space rugosity are not studied;

3, the interpretation of the PP reflection results in terms of weak anisotropic reflection coefficient may reveal more about the practical relationship between friability and Thomsen's parameters if the anisotropy is weak;

4, different values of crack density, aspect ratio, and background stiffness-tensor should be put into the program and the results should be interpreted;

5, the Biot and PVE theories are all frequency-dependent and attenuative, but our GSA modeling is not. It would be useful if we can develop GSA into a frequency-dependent theory with ellipsoid inclusions, then compare them in the same frequency band (Chesnokov et al., 1998);

6, the GSA modeling results are polar angle dependent and azimuthally anisotropic. Nonetheless, the Biot and PVE theories are not. An averaging procedure or other technique needs to be applied to the modeling results, so the uncertainties that influence the comparison of pore connectivity are as few as possible;

7, application of the two theoretical frames to the same rock is strongly recommended;

8, the application of propagator matrix method to multilayered anisotropic and poroelastic media since real earth is multilayered.

Bibliography

Agersborg, R. T., A. Johansen, and B. O. Ruud, 2008, Modeling reflection signatures of pore fluids and dual porosity in carbonate reservoirs: Journal of Seismic Exploration, **17**, 1514–1518.

Aki, K., and P. G. Richards, 2009, Quantitative seismology: University Science Books.

Ayzenberg, M. A., A. M. Aizenberg, H. B. Helle, K. D. Klem-Musatov, J. Pajchel, and B. Ursin, 2007, 3D diffraction modeling of singly scattered acoustic wavefields based on the combination of surface integral propagators and transmission operators: Geophysics, **72**, SM19–SM34.

Bayuk, I., and E. Chesnokov, 1998, Correlation between elastic and transport properties of porous cracked anisotropic media: Physics and Chemistry of the Earth, **23**, 361–366.

Bayuk, I., and M. Rodkin, 1999, Modeling of a medium with hierarchic microcrack structure by the general singular approximation method: Physics of the Earth and Planetary Interiors, **114**, 15–24.

Bayuk, I. O., M. Ammerman, and E. M. Chesnokov, 2007, Elastic moduli of anisotropic clay: Geophysics, **72**, D107–D117.

———, 2008, Upscaling of elastic properties of anisotropic sedimentary rocks: Geophysical Journal International, **172**, 842–860.

Berryman, J. G., 1980, Confirmation of Biot's theory: Applied Physics Letters, **37**, 382.

Beyer, W., 1991, Standard mathematical tables and formulae: CRC Press.

Biot, M. A., 1956a, Theory of propagation of elastic waves in a fluid-saturated porous solid. I. Low-frequency range: Journal of the Acoustical Society of America, **28**, 168–178.

———, 1956b, Theory of propagation of elastic waves in a fluid-saturated porous solid. II. Higher frequency range: Journal of the Acoustical Society of America, **28**, 179–191.

———, 1962, Mechanics of deformation and acoustic propagation in porous media: Journal of Applied Physics, **33**, 1482–1498.

Born, W., 1941, The attenuation constant of earth materials: Geophysics, **6**, 132–148.

Bourbie, T., O. Coussy, and B. Zinszner, 1987, Acoustics of porous media: Gulf Publishing Company.

Bouzidi, Y., and D. R. Schmitt, 2012, Incidence-angle-dependent acoustic reflections from liquid-saturated porous solids: Geophysical Journal International, **191**, 1427–1440.

Carcione, J. J. M., 2007, Wave fields in real media: Wave propagation in anisotropic, anelastic, porous and electromagnetic media: Elsevier.

Carcione, J. M., 1998, Viscoelastic effective rheologies for modelling wave propagation in porous media: Geophys. Prosp., **46**, 249–270.

Carcione, J. M., and H. B. Helle, 1999, Numerical solution of the poroviscoelastic wave equation on a staggered mesh: Journal of Computational Physics, **154**, 520–527.

Chattopadhyay, A., 2006, Wave reflection and refraction in triclinic crystalline media: Archive of Applied Mechanics, **76**, 65–74.

Chen, H., 2000, Anisotropic effects upon amplitude-vs-offset response in realistic earth models: PhD thesis, University of Oklahoma.

Chesnokov, E., Y. A. Kukharenko, and P. Y. Kukharenko, 1998, Frequency dependence of physical parameters of microinhomogeneous media. space statistics: Revue de l Institut Francais du Petrole, **53**, 729–734.

Denneman, A. I. M., G. G. Drijkoningen, D. M. J. Smeulders, and K. Wapenaar, 2002, Reflection and transmission of waves at a fluid/porous-medium interface: Geophysics, **67**, 282–291.

Deresiewicz, H., 1960, The effect of boundaries on wave propagation in a liquid-filled porous solid: I. Reflection of plane waves at a free plane boundary (non-dissipative case): Bulletin of the Seismological Society of America, **50**, 599–607.

Deresiewicz, H., and R. Skalak, 1963, On uniqueness in dynamic poroelasticity: Bulletin of the Seismological Society of America, **53**, 783–788.

Domenico, S. N., 1974, Effect of water saturation on seismic reflectivity of sand reservoirs encased in shale: Geophysics, **39**, 759–769.

Downton, J. E., and C. Ursenbach, 2006, Linearized amplitude variation with offset (AVO) inversion with supercritical angles: Geophysics, **71**, E49–E55.

Dutta, N. C., and H. Ode, 1979, Attenuation and dispersion of compressional-waves in fluid-filled rocks with partial gas saturation (White model) - Part II: Results: Geophysics, **44**, 1789–1805.

———, 1983, Seismic reflections from a gas-water contact: Geophysics, **48**, 148–162.

Dvorkin, J., and A. Nur, 1993, Dynamic poroelasticity: A unified model with the squirt and the Biot mechanism: Geophysics, **58**, 524–533.

Eshelby, J. D., 1957, The determination of the elastic field of an ellipsoidal inclusion, and related problems: Proceedings of the Royal Society of London. Series A. Mathematical and Physical Sciences, **241**, 376–396.

Fokin, A. G., 1973, Singular approximation for the calculation of the elastic properties of reinforced systems: Mechanics of Composite Materials, **9**, 445–449.

Geertsma, J., and D. C. Smit, 1961, Some aspects of elastic wave propagation in fluid-saturated porous solids: Geophysics, **26**, 169–181.

Grechka, V., 2002, On-line at: http://www.cwp.mines.edu/cwpmatlab/cwpmatlab.tgz.

Green, G., 1848, On the laws of the reflexion and refraction of light at the common surface of two non-crystallized media: Transactions of the Cambridge Philosophical Society, **7**, 1.

Hilterman, F. J., 2001, Seismic amplitude interpretation: 2001 distinguished instructor short course: SEG Books.

Hovem, J. M., and G. D. Ingram, 1979, Viscous attenuation of sound in saturated sand: Journal of the Acoustical Society of America, **66**, 1807–1812.

Hudson, J. A., 1981, Wave speeds and attenuation of elastic waves in material containing cracks: Geophysical Journal of the Royal Astronomical Society, **64**, 133–150.

Jakosky, J. J., 1950, Exploration geophysics: Trija Publishing Company.

Jiang, T., 2013, Connection of elastic and transport properties: Effective medium study in anisotropic porous media: PhD thesis, University of Houston.

Jiang, T., and E. M. Chesnokov, 2012, Elastic moduli's relation to microstructure properties in porous media using GSA modeling: 82th Annual International Meeting, SEG, Expanded Abstracts.

Jones, L. E., and H. F. Wang, 1981, Ultrasonic velocities in cretaceous shales from the Williston basin: Geophysics, **46**, 288–297.

Keith, C. M., and S. Crampin, 1977, Seismic body waves in anisotropic media: Reflection and refraction at a plane interface: Geophysical Journal of the Royal Astronomical Society, **49**, 181–208.

Keys, R. G., and S. Xu, 2002, An approximation for the Xu-White velocity model: Geophysics, **67**, 1406–1414.

Knott, C. G., 1888, Reflexion and refraction of elastic waves, with seismological applications: *in* M. A. Pelissier, H. Hoeber, N. van de Coevering, and I. F. Jones, eds., Classics of elastic wave theory: SEG, 261-286.

Koefoed, O., 1955, On the effect of Poisson's ratios of rock strata on the reflection coefficients of plane-waves: Geophys. Prosp., **03**, 381–387.

———, 1962, Reflection and transmission coefficients for plane longitudinal incident waves: Geophys. Prosp., **10**, 304–351.

Krebes, E., and P. Daley, 2007, Difficulties with computing anelastic plane-wave reflection and transmission coefficients: Geophysical Journal International, **170**, 205–216.

Kuster, G. T., and M. N. Toksöz, 1974, Velocity and attenuation of seismic waves in two-phase media - Part I: Theoretical formulations: Geophysics, **39**, 587–606.

Landrø, M., and I. Tsvankin, 2007, Seismic critical-angle reflectometry: A method to characterize azimuthal anisotropy?: Geophysics, **72**, D41–D50.

Levin, F. K., 1986, When reflection coefficients are zero: Geophysics, **51**, 736–741.

Li, Y., W. Han, C.-s. Chen, T. Huang, et al., 2012, Velocity model building for tilted orthorhombic depth imaging: 82th Annual International Meeting, SEG, Expanded Abstracts.

Li, Y., Q. Wu, Z. Li, and W. Han, 2013, Tilted orthorhombic imaging for full azimuth towed streamer data in deep water Gulf of Mexico: 75th Conference & Technical Exhibition, EAGE, Extended Abstracts.

Liner, C. L., 2012, Elements of seismic dispersion: A somewhat practical guide to frequency-dependent phenomena: SEG Books.

Lu, K., 2012, Gas shale permeability and velocity measurement at laboratory scale: Master's thesis, University of Houston.

Mavko, G., T. Mukerji, and J. Dvorkin, 2003, The rock physics handbook: Tools for seismic analysis of porous media: Cambridge University Press.

Müller, T. M., B. Gurevich, and M. Lebedev, 2010, Seismic wave attenuation and dispersion resulting from wave-induced flow in porous rocks - A review: Geophysics, **75**, 75A147–75A164.

Ostrander, W. J., 1984, Plane-wave reflection coefficients for gas sands at nonnormal angles of incidence: Geophysics, **49**, 1637–1648.

Pride, S. R., J. M. Harris, D. L. Johnson, A. Mateeva, K. T. Nihel, R. L. Nowack, J. W. Rector, H. Spetzler, R. Wu, T. Yamomoto, et al., 2003, Permeability dependence of seismic amplitudes: The Leading Edge, **22**, 518–525.

Quintal, B., S. M. Schmalholz, and Y. Y. Podladchikov, 2011, Impact of fluid saturation on the reflection coefficient of a poroelastic layer: Geophysics, **76**, N1–N12.

Rasolofosaon, P. N., 1988, Importance of interface hydraulic condition on the generation of second bulk compressional wave in porous media: Applied Physics Letters, **52**, 780–782.

Rasolofosaon, P. N. J., 1991, Plane acoustic waves in linear viscoelastic porous media: Energy, particle displacement, and physical interpretation: Journal of the Acoustical Society of America, **89**, 1532–1550.

Rathore, J. S., E. Fjaer, R. M. Holt, and L. Renlie, 1994, P-and S-wave anisotropy of a synthetic sandstone with controlled crack geometry: Geophys. Prosp., **43**, 711–728.

Rubino, J., D. R. Velis, and H. Klaus, 2012, Permeability effects on the seismic response of gas reservoirs: Geophysical Journal International, **189**, 448–468.

Rüger, A., 1998, Variation of P-wave reflectivity with offset and azimuth in anisotropic media: Geophysics, **63**, 935–947.

Santos, J., J. Corbero, C. Ravazzoli, and J. Hensley, 1992, Reflection and transmission coefficients in fluid-saturated porous media: Journal of the Acoustical Society of America, **91**, 1911–1923.

Sayers, C., 1994, P-wave propagation in weakly anisotropic media: Geophysical Journal International, **116**, 799–805.

Schoenberg, M., and J. Protazio, 1992, Zoeppritz rationalized and generalized to anisotropy: Journal of Seismic Exploration, **1**, 125–144.

Shermergor, T. D., 1977, Theory of elasticity of microinhomogeneous media: Nauka.

Shuey, R. T., 1985, A simplification of the Zoeppritz equations: Geophysics, **50**, 609–614.

Sil, S., and M. K. Sen, 2009, Seismic critical-angle anisotropy analysis in the τ-p domain: Geophysics, **74**, A53–A57.

Silin, D., and G. Goloshubin, 2010, An asymptotic model of seismic reflection from a permeable layer: Transport in porous media, **83**, 233–256.

Skopintseva, L., M. Ayzenberg, M. Landrø, T. Nefedkina, and A. M. Aizenberg, 2011, Long-offset AVO inversion of PP reflections from plane interfaces using effective reflection coefficients: Geophysics, **76**, C65–C79.

Spencer Jr, J. W., 1981, Stress relaxations at low frequencies in fluid-saturated rocks: Attenuation and modulus dispersion: Journal of Geophysical Research, **86**, 1803–1812.

Stoll, R. D., and T. K. Kan, 1981, Reflection of acoustic waves at a water–sediment interface: Journal of the Acoustical Society of America, **70**, 149–156.

Sun, Y. F., 2004, Pore structure effects on elastic wave propagation in rocks: AVO modelling: Journal of Geophysics and Engineering, **1**, 268–276.

Tao, G., M. S. King, and M. Nabi-Bidhendi, 1995, Ultrasonic wave propagation in dry and brine-saturated sandstones as a function of effective stress: Laboratory measurements and modelling: Geophys. Prosp., **43**, 299–327.

Thomsen, L., 1986, Weak elastic anisotropy: Geophysics, **51**, 1954–1966.

Tisato, N., and B. Quintal, 2013, Measurements of seismic attenuation and transient fluid pressure in partially saturated Berea sandstone: evidence of fluid flow on the mesoscopic scale: Geophysical Journal International, **195**, 342–351.

Tiwary, D., 2007, Mathematical modeling and ultrasonic measurement of shale anisotropy and a comparison of upscaling methods from sonic to seismic: PhD thesis, University of Oklahoma.

Toksöz, M. N., D. H. Johnston, and A. T. Timur, 1979, Attenuation of seismic waves in dry and saturated rocks - I. Laboratory measurements: Geophysics, **44**, 681–690.

Tsvankin, I., 1997a, Anisotropic parameters and P-wave velocity for orthorhombic media: Geophysics, **62**, 1292–1309.

———, 1997b, Reflection moveout and parameter estimation for horizontal transverse isotropy: Geophysics, **62**, 614–629.

———, 2005, Seismic signatures and analysis of reflection data in anisotropic media: Elsevier Science.

Tsvankin, I., and E. Chesnokov, 1990, Synthesis of body wave seismograms from point sources in anisotropic media: Journal of Geophysical Research, **95**, 11317–11331.

Ursin, B., and A. Stovas, 2002, Reflection and transmission responses of a layered isotropic viscoelastic medium: Geophysics, **67**, 307–323.

Vavrycuk, V., and I. Psencik, 1998, PP-wave reflection coefficients in weakly anisotropic elastic media: Geophysics, **63**, 2129–2141.

Winterstein, D. F., and J. B. Hanten, 1985, Supercritical reflections observed in P-wave and S-wave data: Geophysics, **50**, 185–195.

Wu, K., Q. Xue, and L. Adler, 1990, Reflection and transmission of elastic waves from a fluid-saturated porous solid boundary: Journal of the Acoustical Society of America, **87**, 2349–2358.

Yang, J., 1999, Importance of flow condition on seismic waves at a saturated porous solid boundary: Journal of Sound and Vibration, **221**, 391–413.

Yang, J., and T. Sato, 1998, Influence of viscous coupling on seismic reflection and transmission in saturated porous media: Bulletin of the Seismological Society of

America, **88**, 1289–1299.

———, 2000, Effects of pore-water saturation on seismic reflection and transmission from a boundary of porous soils: Bulletin of the Seismological Society of America, **90**, 1313–1317.

Young, G. B., and L. W. Braile, 1976, A computer program for the application of Zoeppritz's amplitude equations and Knott's energy equations: Bulletin of the Seismological Society of America, **66**, 1881–1885.

Zhu, X., and G. A. McMechan, 2012, Elastic inversion of near-and postcritical reflections using phase variation with angle: Geophysics, **77**, R149–R159.

Zoeppritz, K., 1919, On the reflection and transmission of seismic waves at surfaces of discontinuity: *in* M. A. Pelissier, H. Hoeber, N. van de Coevering, and I. F. Jones, eds., Classics of elastic wave theory: SEG, 363-376.